

AD-R143 185

THE INFLUENCE OF HIGH ANGLE OF ATTACK FLOW PHENOMENA ON THE DYNAMIC STABI. (U) NOTRE DAME UNIV IN DEPT OF AEROSPACE AND MECHANICAL ENGINEER.

1/1

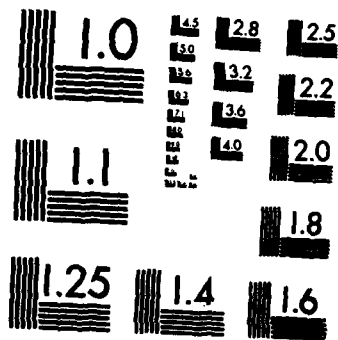
UNCLASSIFIED

J M JENISTA ET AL. JAN 83 AFATL-TR-83-04

F/G 20/4

NL





MICROCOPY RESOLUTION TEST CHART
NATIONAL BUREAU OF STANDARDS-1963-A

AD 1800 ?

AD-A143 185

(A)

AFATL-TR-83-04

The Influence of High Angle of Attack Flow Phenomena on the Dynamic Stability of Slender Missiles

James M Jenista
Robert C Nelson

UNIVERSITY OF NOTRE DAME
AEROSPACE & MECHANICAL ENGINEERING DEPARTMENT
NOTRE DAME, INDIANA 46556

JANUARY 1983

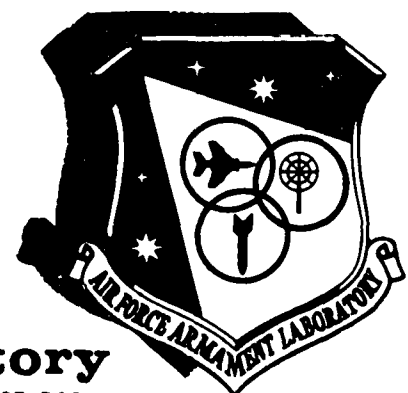
FINAL REPORT FOR PERIOD JULY 1980—AUGUST 1982

DTIC

JUL 18 1984

DTIC FILE COPY

Approved for public release; distribution unlimited



Air Force Armament Laboratory

AIR FORCE SYSTEMS COMMAND * UNITED STATES AIR FORCE * EGLIN AIR FORCE BASE, FLORIDA

84 07 16 072

NOTICE

**Please do not request copies of this report from the Air Force Armament Laboratory.
Additional copies may be purchased from:**

**National Technical Information Service
5285 Port Royal Road
Springfield, Virginia 22161**

**Federal Government agencies and their contractors registered with Defense Technical
Information Center should direct requests for copies of this report to:**

**Defense Technical Information Center
Cameron Station
Alexandria, Virginia 22314**

UNCLASSIFIED

SECURITY CLASSIFICATION OF THIS PAGE (When Data Entered)

REPORT DOCUMENTATION PAGE		READ INSTRUCTIONS BEFORE COMPLETING FORM
1. REPORT NUMBER AFATL-TR-83-04	2. GOVT ACCESSION NO. AD A143185	3. RECIPIENT'S CATALOG NUMBER
4. TITLE (and Subtitle) THE INFLUENCE OF HIGH ANGLE OF ATTACK FLOW PHENOMENA ON THE DYNAMIC STABILITY OF SLENDER MISSILES		5. TYPE OF REPORT & PERIOD COVERED Final Report: July 1980 - August 1982
		6. PERFORMING ORG. REPORT NUMBER
7. AUTHOR(s) James M. Jenista Robert C. Nelson		8. CONTRACT OR GRANT NUMBER(s) FO8635-80-K-0303
9. PERFORMING ORGANIZATION NAME AND ADDRESS Aerospace and Mechanical Engineering Department University of Notre Dame Notre Dame, Indiana 46556		10. PROGRAM ELEMENT, PROJECT, TASK AREA & WORK UNIT NUMBERS PE: 61102F JON: 2307-E1-14
11. CONTROLLING OFFICE NAME AND ADDRESS Air Force Armament Laboratory (DLMA) Armament Division Eglin Air Force Base, Florida 32542		12. REPORT DATE January 1983
14. MONITORING AGENCY NAME & ADDRESS (if different from Controlling Office)		13. NUMBER OF PAGES 69
		15. SECURITY CLASS. (of this report) Unclassified
16. DISTRIBUTION STATEMENT (of this Report) Approved for public release; distribution unlimited.		15a. DECLASSIFICATION, DOWNGRADING SCHEDULE
17. DISTRIBUTION STATEMENT (of the abstract entered in Block 20, if different from Report)		
18. SUPPLEMENTARY NOTES Availability of this report is specified on verso of front cover.		
19. KEY WORDS (Continue on reverse side if necessary and identify by block number) Missile Aerodynamics Body Vortices High Angle of Attack Flow Visualization Separated Flow		
20. ABSTRACT (Continue on reverse side if necessary and identify by block number) The purpose of this study was to gain a better understanding of the influence of the separated wake flows on vehicle dynamic stability. This was accomplished by mapping out the body vortex wake flow around several slender missile configurations using flow visualization techniques. Two techniques were employed, one using a laser-produced sheet of light illuminating smoke passing around the model, and the other using neutrally buoyant helium-filled soap bubbles as flow tracers.		

DD FORM 1473
1 JAN 73

EDITION OF 1 NOV 65 IS OBSOLETE

UNCLASSIFIED

SECURITY CLASSIFICATION OF THIS PAGE (When Data Entered)

UNCLASSIFIED

SECURITY CLASSIFICATION OF THIS PAGE(When Data Entered)

20. ABSTRACT (CONCLUDED)

The models were tested at angles of attack from 15 to 55 degrees, at sub-critical Reynolds numbers and for freestream turbulence levels of 0.1 to 0.8 percent. The body vortices were observed to assume positions relative to the models that were either steady and symmetric, steady and asymmetric, or unsteady and asymmetric. The wake structure was found too sensitive to model surface roughness and freestream turbulence.

UNCLASSIFIED

SECURITY CLASSIFICATION OF THIS PAGE(When Data Entered)

PREFACE

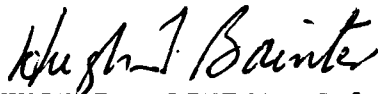
This report was prepared by the Aerospace and Mechanical Engineering Department at the University of Notre Dame, Notre Dame, Indiana 46556, under Contract No. F08635-80-K-0303 with the Air Force Armament Laboratory, Armament Division, Eglin Air Force Base, Florida 32542. Mr Carroll B. Butler (DLMA) monitored the program for the Armament Laboratory. This effort was conducted during the period from July 1980 to August 1982.

The authors wish to express their appreciation to Dr Donald C. Daniel and Mr Carroll B. Butler of the Air Force Armament Laboratory for their comments and suggestions during the course of this investigation and to the Air Force Office of Scientific Research (AFOSR) for sponsoring the effort.

This report has been reviewed by the Public Affairs Office and is releasable to the National Technical Information Service (NTIS), where it will be available to the general public, including foreign nationals.

This technical report has been reviewed and is approved for publication.

FOR THE COMMANDER



HUGH T. BAINTER, Colonel, USAF
Chief, Guided Weapons Division

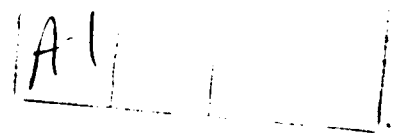


TABLE OF CONTENTS

Section	Title	Page
I	INTRODUCTION	1
II	DYNAMIC STABILITY PARAMETERS AT LARGE ANGLES OF ATTACK	3
	2.1 Introduction	3
	2.2 A Review of Static Aerodynamic Phenomena	4
	2.3 Dynamic Sensitivity Studies	10
III	EXPERIMENTAL STUDY	14
	3.1 Introduction	14
	3.2 Laboratory Arrangement	15
	3.3 Wind Tunnel Models	15
	3.4 Wind Tunnel	15
	3.5 Smoke Generation	20
	3.6 Sheet of Light	22
	3.7 Bubble Generation.	22
	3.8 Lighting	24
	3.9 Photography	25
	3.10 General Procedure	26
	3.11 Vortex Mapping	27
	3.12 Bubble Visualization	29
IV	DISCUSSION OF EXPERIMENTAL RESULTS	31
	4.1 Vortex Mapping	31
	4.2 Laser Smoke Flow Visualization	32
	4.3 Helium Bubble Visualization	53
	4.4 Influence of Roughness and Freestream Turbulence	53
V	CONCLUSIONS.	57
VI	RECOMMENDATIONS	59

LIST OF FIGURES

Figure	Title	Page
1	High Angle of Attack Dynamic Stability Data From Reference 5	5
2	Asymmetric Vortex Flow Field.	8
3	The Effect of Reynolds Number on Maximum Side Force at $\alpha = 55^\circ$ Ogive-Cylinder, $L_N/D = 2$, Reference 3	8
4	Vortex Burst Point on Delta Wing Models	9
5	Vortex Burst Point versus Sweep Angle	9
6	Vortex Burst Point for Varying Side Slip Angle	10
7	Root Locus Plot Showing the Effect of $C_{\ell q}$ on Open Loop Roots of a Yaw-to-Turn Missile Reference 21.	12
8	Sketch of Wind Tunnel Model and Grid Scale.	16
9	Sketch of Laser and Wind Tunnel Arrangement	17
10	Flow Visualization Models	18
11	Univeristy of Notre Dame's Subsonic Wind Tunnel.	19
12	Smoke Generator	21
13	Smoke Rake	21
14	Laser and Lens Setup.	23
15	Bubble Generator	23
16	Non-Dimensional Vortex Trajectory Data, Z/r_b vs $\alpha x / r$	33
17	Non-Dimensional Vortex Trajectory Data y/r_b vs $\alpha x / r$	33
18	Vortex Pattern on the NAE Model at $\alpha = 25^\circ$	34
19	Vortex Pattern on the NAE Model at $\alpha = 35^\circ$	35

LIST OF FIGURES (CONTINUED)

Figure	Title	Page
20	Vortex Pattern on NAE Model at $\alpha = 45^\circ$	36
21	Vortex Pattern on NAE Model at $\alpha = 50^\circ$	37
22	Vortex Pattern on NAE Model at $\alpha = 55^\circ$	38
23	Vortex Pattern on Tangent Ogive Nose Model $\alpha = 25^\circ$	39
24	Vortex Pattern on Tangent Ogive Nose Model $\alpha = 35^\circ$	40
25	Vortex Pattern on Tangent Ogive Nose Model $\alpha = 45^\circ$	41
26	Vortex Pattern on Tangent Ogive Nose Model $\alpha = 50^\circ$	42
27	Vortex Pattern on Tangent Ogive Nose Model $\alpha = 55^\circ$	43
28	Vortex Pattern on the Basic Finner Model $\alpha = 25^\circ$	44
29	Vortex Pattern on the Basic Finner Model $\alpha = 35^\circ$	45
30	Vortex Pattern on the Basic Finner Model $\alpha = 45^\circ$	46
31	Vortex Pattern on the Basic Finner Model $\alpha = 50^\circ$	47
32	Vortex Pattern on the Basic Finner Model $\alpha = 55^\circ$	48
33	Enlargement of Vortical Flow Structure on NAE Model	49
34	Enlargement of Vortical Flow Structure on Tangent Ogive Nose Model.	50
35	Enlargement of Vortical Flow Structure on Basic Finner Model	51

LIST OF FIGURES (CONCLUDED)

Figure	Title	Page
36	Helium Bubble Photograph of the Wake Around the Fins of the NAE Model	52
37	Turbulence Intensity in the Test Section due to Wire Screens	55

LIST OF TABLES

Table	Title	Page
1	Problem Areas Associated with High Angle of Attack Dynamic Stability Testing.	2
2	Dynamic Derivatives Measured at Large Angles of Attack.	3
3	Summary of Missile Sensitivity Study by T. F. Langham.	13
4	Geometric Data for Selected Body Stations.	29

SECTION I

INTRODUCTION

Modern high performance aircraft and missiles must have the capability to maneuver rapidly if they are to be effective in performing their intended mission. Maneuverability can be achieved by increasing the force normal to the vehicle's flight path. For lifting body configurations, the high g maneuver can be accomplished at relatively low angles of incidence but at large angular rates. On the other hand, slender high fineness ratio configurations achieve their maneuverability by flying at large angles of incidence and angular rates. Both types of configurations can experience non-linear aerodynamic interactions due to flow separation.

Starting in the early 1970's there was a renewed interest in high angle of attack aerodynamics. Numerous experimental studies were conducted to examine the flow field surrounding slender bodies of revolution. Of particular interest to researchers were the asymmetric body vortex wake flows. This complicated flow structure was shown to give rise to significant out-of-plane forces and moments for a symmetric flight condition, i.e., $\beta = 0$. Much progress has been made in understanding the complicated flow structure at large angles of attack.¹⁻⁴

Although much has been learned about the static aerodynamics of missile configurations at large angles of attack, our understanding of how these complicated vortex wake flows affect the vehicle's dynamic stability characteristics is quite limited. To improve the understanding of dynamic characteristics of missiles undergoing large angular rate maneuvers at low and high angles of attack requires a comprehensive dynamic stability research program be undertaken. However, before such a research program can be started a variety of problems must be addressed. Some of the problems associated with high angle of attack dynamic testing include; model

configuration sensitivity, Reynolds number effects and support interference. Table 1 gives a more detailed summary of these potential difficulties.

It was the goal of this research investigation to examine these difficulties and to develop recommendations for their solution. A second and more substantial part of this study dealt with an experimental investigation of the flow field surrounding two models which have been, or in the near future will be, used in high angle of attack dynamic stability research efforts.

TABLE 1. PROBLEM AREAS ASSOCIATED WITH HIGH ANGLE OF ATTACK DYNAMIC STABILITY TESTING

Configuration Sensitivity	Small geometric changes can result in large aerodynamic changes.
Reynolds Number Effects	Aerodynamic characteristics at large angles of attack are dominated by separated flow behavior which can be highly dependent upon Reynolds number.
Support Interference	Downstream support systems have been shown to cause interference with the leeward wake structure.
Non-linear Aerodynamics	Vortices created by the body or lifting surfaces can produce non-linear aerodynamic interactions.
Cross-Coupling	Asymmetric vortex wake structure can cause aerodynamic coupling between longitudinal and lateral degrees of freedom.

SECTION II
 DYNAMIC STABILITY PARAMETERS AT LARGE
 ANGLES OF ATTACK

2.1 Introduction

Until recently very little attention has been given to the effect that high angle of attack flight might have on dynamic stability parameters. Most of the high angle of attack research has dealt with static aerodynamic phenomena. However, recent dynamic wind tunnel experiments have shown that there can be large increases in the magnitude of direct derivatives and the presence of cross-coupling derivatives that may be important for accurate simulation studies. Table 2 is a summary of the dynamic derivatives that have been measured on missile configurations at large angles of attack.

When the angle of attack exceeds 10 degrees, the leeward side separated flow fields can cause non-linear static and dynamic aerodynamic characteristics. The flow asymmetry due to the asymmetric vortex shedding can lead to significant aerodynamic cross-coupling between longitudinal and lateral motions of the missile.

TABLE 2. DYNAMIC DERIVATIVES MEASURED AT
 LARGE ANGLES OF ATTACK

<u>Direct Derivatives</u>	<u>Cross Derivatives</u>	<u>Cross-Coupling Derivatives</u>
$C_{m_q}, C_{n_r}, C_{\dot{\alpha}_p}$	$C_{\dot{\alpha}_r}, C_{n_p}$	C_{m_p}, C_{m_r}
$C_{m_{\dot{\alpha}}}, C_{L_q}, C_{L_{\dot{\alpha}}}$	C_{y_r}, C_{y_p}	$C_{\dot{\alpha}_q}, C_{n_q}$

New balances suitable for measuring dynamic derivatives at large angles of attack have been developed in Canada at the National Aeronautical Establishment (NAE) and in the United States at the Arnold Engineering Development Center (AEDC). Wind tunnel experiments using these new balances

have shown some very interesting results. Using a dynamic balance capable of measuring the direct derivatives [$C_{m_q} + C_{m_{\dot{\alpha}}}$, $C_{n_r} - C_{n_{\dot{\beta}}}$ etc.], as well as the cross-derivatives such as $C_{m_{\dot{\beta}}}$ and $C_{n_q} + C_{n_{\dot{\alpha}}}$, a test was conducted to determine the dynamic characteristics of a wing-body configuration at large angles of attack⁵. The model was tested for angles of attack from 0 to 40 degrees and for Mach numbers of 0.25 and 0.7. The dynamic derivatives due to pitching and yawing oscillations $C_{m_q} + C_{m_{\dot{\alpha}}}$ and $C_{n_r} - C_{n_{\dot{\beta}}}$ $\cos \alpha_0$ at large angles of attack were found to be eight times greater than the low angle of attack measurements. Significant cross-coupling derivatives were also found, for example, $C_{n_q} + C_{n_{\dot{\alpha}}}$ was nearly twice as large as $C_{n_r} - C_{n_{\dot{\beta}}}$ $\cos \alpha_0$ in the high angle of attack regime. Figure 1 shows a sketch of the model and some of the dynamic stability measurements.

2.2 A Review of Static Aerodynamic Phenomena

The influence of high angle of attack aerodynamic phenomena on aircraft and missile dynamic stability characteristics was the subject of two recent AGARD lecture series⁸⁻⁹. To gain some insight into the implication of high angle of attack flight on dynamic stability parameters it is appropriate to first review the static aerodynamic phenomena in this regime. Of particular interest are the studies dealing with asymmetric body vortex flows and vortex bursting. Each of these phenomenon can affect the dynamic behavior of a missile as it executes a high performance maneuver. The body vortex formation and its interaction with other components of the missile have received considerable research interest during the past decade. In the case of either an aircraft having a long slender forebody or a high fineness ratio missile, the forebody vortices can become asymmetric as the angle of attack is increased. The asymmetric disposition of the vortices gives rise to significant side force and yawing moments because of the flow asymmetry. The problem can become more complicated if the asymmetric vortex

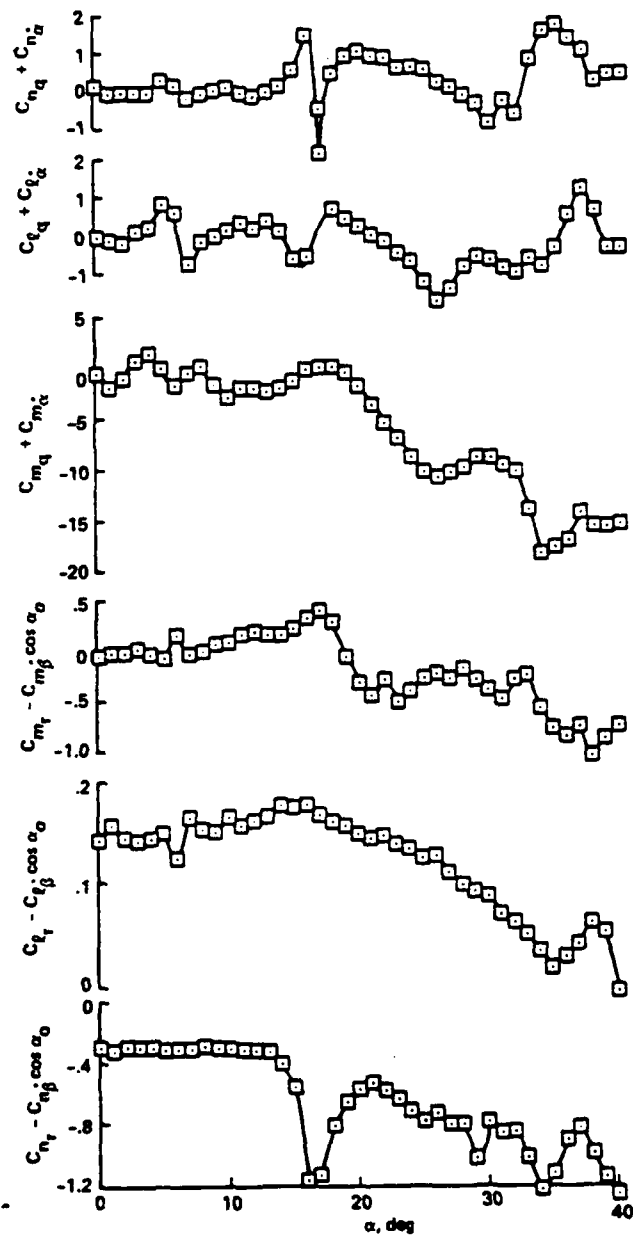


Figure 1. High Angle of Attack Dynamic Stability Data From Reference 5

wake interacts with aft lifting surfaces such as wings or tail planes.

Figure 2 is a sketch of the complicated flow field that can be experienced by a slender missile configuration at large angles of attack.

An excellent summary of the state of understanding regarding asymmetric vortex wakes and their associated forces and moments was presented recently in a paper by Hunt¹. He concluded his paper with an assessment of what is known and what remains to be understood regarding asymmetric vortex wakes.

Asymmetric vortex wake flows are extremely sensitive to freestream turbulence, model fidelity, nose geometry and Reynolds number. The maximum asymmetric loads occur when the boundary layer flow is either completely laminar or completely turbulent. If the boundary layer flow is transitional, one can usually expect to find the lowest vortex induced side force. The influence of Reynolds number is clearly illustrated in Figure 3.

When testing models at high angles of attack one should avoid the transitional Reynolds number range, freestream turbulence level should be low and the model support should be rigid. High angle of attack data is quite sensitive to support interference and great care must be taken to ensure the support system does not alter the wake flow¹⁰⁻¹³.

Another aerodynamic problem at large angles of attack is the bursting of leading edge vortices on delta wing configurations or highly swept wings having leading edge extensions. As the angle of attack increases, the leading edge vortex undergoes a dramatic change. The axial velocity within the vortex goes to zero, the diameter increases and the circumferential velocity decreases. This sudden change in the vortex structure is referred to as vortex breakdown or vortex bursting.

The vortex burst location is a function of the sweep angle and is illustrated in Figures 4 and 5. For a given sweep angle the burst point moves toward the apex as the angle of attack increases. The larger the

sweep angle the higher the angle of attack must be before the burst point reaches the trailing edge. Figure 6 shows the effect of side slip on the vortex burst location. As illustrated in this figure, the windward vortex will burst earlier.

As illustrated in Figure 6, the vortex burst location is very sensitive to small changes in side slip angle. It has been observed experimentally that at large angles of attack the symmetric vortex pattern is unstable to small perturbations in side slip. A small perturbation can cause an asymmetric bursting of the vortices which, in turn, gives rise to a rolling moment and self-induced roll oscillations¹⁸.

As elaborated in this section, there are many difficulties in conducting high angle of attack static aerodynamic testing. The problems of Reynolds number effects, data repeatability, configuration sensitivity and support interference will also cause difficulties for high angle of attack dynamic testing. In addition to these problems, dynamic balances capable of measuring cross-coupling derivatives are highly refined state-of-the-art instruments. They are subject to problems in amplification, calibration and difficulties involved with operating in a high noise environment.

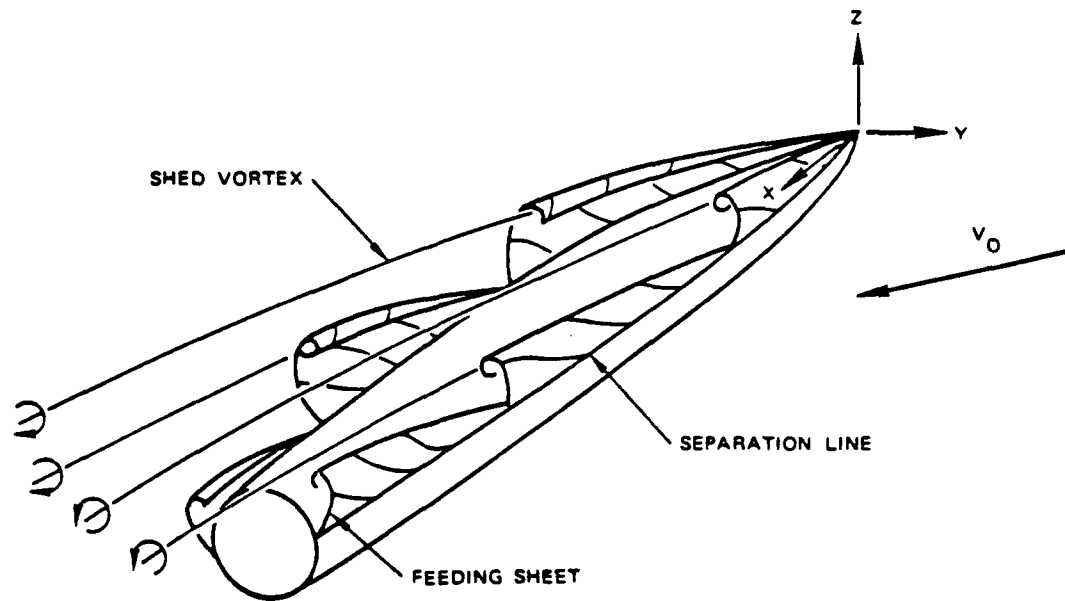


Figure 2. Asymmetric Vortex Flow Field

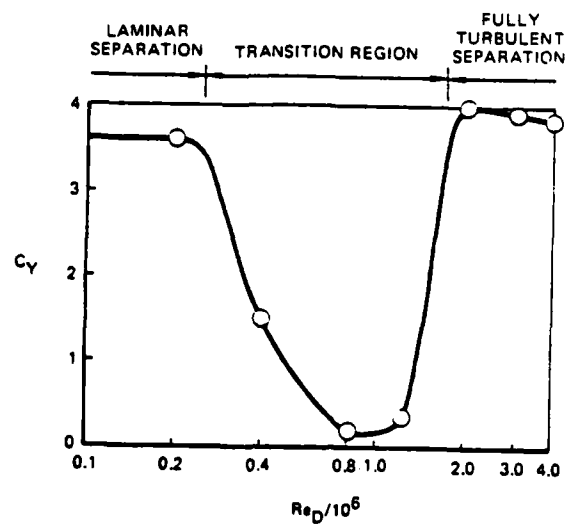


Figure 3. The Effect of Reynolds Number on Maximum Side Force at $\alpha = 55^\circ$ Ogive Cylinder, $L_N/D = 2$, Reference 3

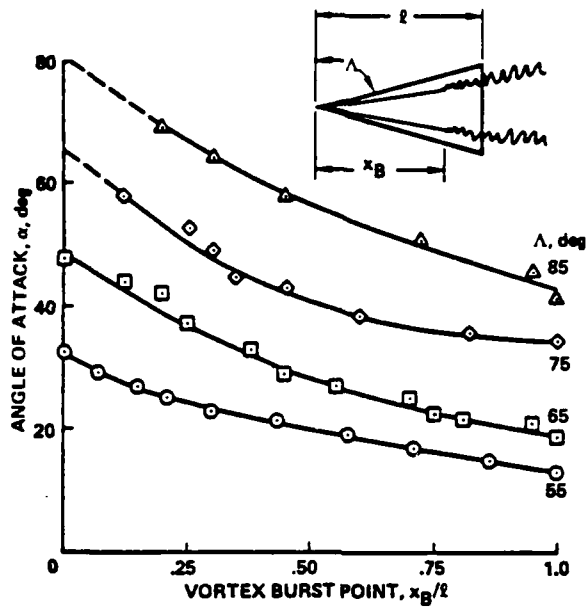


Figure 4. Vortex Burst Point on Delta Wing Models (Reference 17)

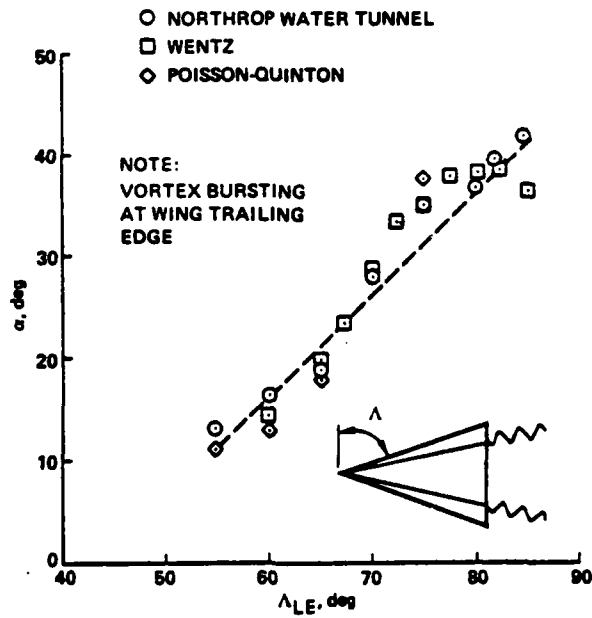


Figure 5. Vortex Burst Point versus Sweep Angle (Reference 17)

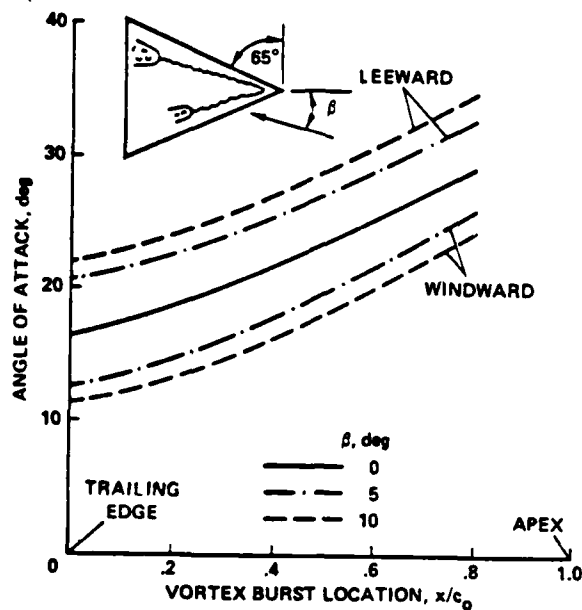


Figure 6. Vortex Burst Point for Varying Side Slip Angle (Reference 17)

2.3 Dynamic Sensitivity Studies

As indicated in the previous section, experimentally measured dynamic derivatives have been found to vary significantly in the high angle of attack regime as compared to the low angle of attack measurements. This is, in general, true for both direct and cross-coupling derivatives.

How these variations in the stability derivatives affect the vehicle's motion is indicated by several analytical studies¹⁹⁻²¹. The study most relevant to this investigation is the one by T. F. Langham²¹. Langham investigated the effect of derivative variation on the open loop characteristics of a bank-to-turn missile and a yaw-to-turn missile. He used a combination of wind tunnel data and predicted derivatives for the two-missile configuration. In the sensitivity analysis, the derivatives were varied by a factor of two to five times the nominal values.

The results of the sensitivity study are summarized in Table 3. One of the more important observations is the effect of the cross-coupling derivatives such as $C_{\ell q}$ on the vehicle's motion. Figure 7 is a root locus plot of the open loop response of a yaw-to-turn missile. The short period and dutch roll modes change significantly with changes in $C_{\ell q}$ and load factor.

These studies have shown that the changes in dynamic derivatives (both direct and cross coupling) can produce large changes in the open loop characteristics of a missile configuration at large angles of attack. What still remains to be accomplished is to assess the effect these dynamic parameters have on the closed loop response.

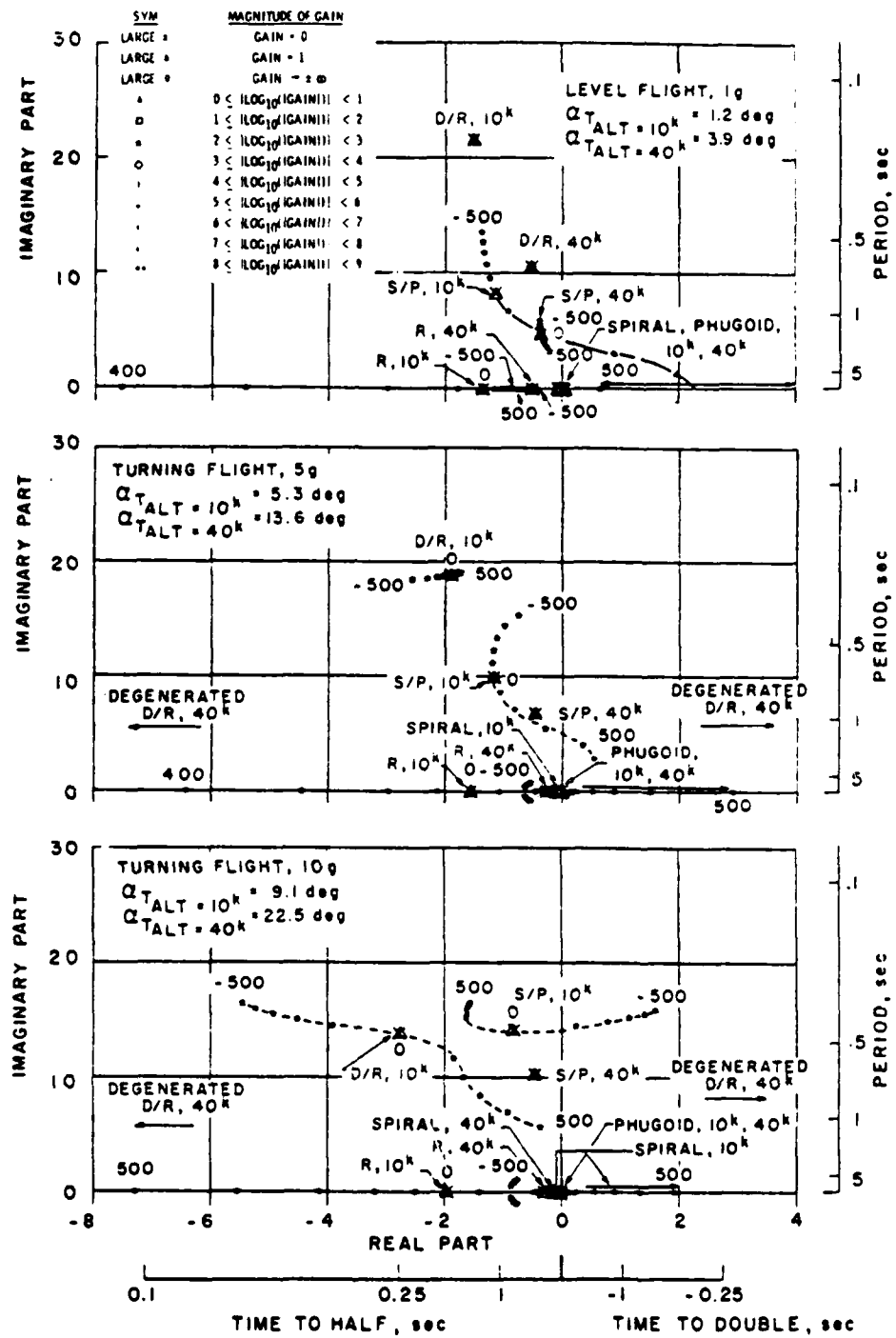


Figure 7. Root Locus Plot Showing the Effect of $C_{\lambda q}$ on Open Loop Roots of a Yaw-to-Turn Missile - Reference 21

TABLE 3. SUMMARY OF MISSILE SENSITIVITY STUDY BY T. F. LANGHAM (REFERENCE 21)

Derivative Variation	Influence of Derivative Variation on Missile Open Loop Response for Either a Bank-to-Turn or Yaw-to-Turn Missile
Longitudinal Direct Derivatives	
$C_m, C_{m\dot{\alpha}}$ C_{nq}	Affects short period damping. Influence diminishes with altitude.
$C_{lq}, C_{l\dot{\alpha}}$	Produces no change in longitudinal or lateral modes.
Lateral Direct Derivatives	
$C_{nr}, C_{nr\dot{p}}$	Roll and dutch roll modes are affected. Both modes are more sensitive to $C_{nr\dot{p}}$ variation.
C_{yr}	No change in longitudinal or lateral modes.
Lateral Cross Derivatives	
$C_{lr}, C_{lr\dot{p}}$	C_{lr} affects dutch roll in a manner similar to the influence of C_{nr} . Roll and dutch roll modes are very sensitive to $C_{nr\dot{p}}$.
C_{yp}	C_{yp} produces only a small change in dutch roll damping.
Cross-Coupling Derivatives	
C_{nq}, C_{nr}	Motion is insensitive to variations.
$C_{mp}, C_{r\dot{q}}$	Short period, phugoid and dutch roll modes are all sensitive to variations in $C_{r\dot{q}}$. Whereas, C_{mp} affects only the short period and dutch roll damping ratios.

SECTION III
EXPERIMENTAL STUDY

3.1 Introduction

One of the primary objectives of this investigation was to broaden the understanding of the relationship between a missile's leeward wake structure and its dynamic stability characteristics. This was accomplished by examining the wake structure on several model configurations for which high angle of attack aerodynamic information is available.

The vortex wake structure was examined primarily through the use of smoke flow visualization. Two techniques were used in an effort to capture the details of various patterns of interest in the flow field. Of corollary importance, then, is the usefulness of the techniques themselves in investigating such flow phenomena. Therefore, in addition to observing and drawing conclusions about the flow itself, detailed descriptions are given and critical analyses are made of the flow visualization techniques, and suggestions are forwarded for their future application.

This study seeks not only to map the location of the vortex cores as a function of the body station and angle of attack, but also to illuminate any secondary flow characteristics. Therefore, visualization techniques were selected that simplify the mapping task and accurately trace the flow patterns.

A laser-produced sheet of light was used for its ability to show a cross-section of the flow. A particular advantage of this technique is the ability to capture both the total smoke pattern and the cross-sectional sheet pattern in a single photograph. Also, the laser light sheet can be tilted so that the sheet is normal to the model's longitudinal axis. This allows the body station and angle of attack to be independent variables during vortex mapping. The remaining two spatial coordinates can then be determined by comparing the vortex core pattern to a superimposed two-dimensional grid at the particular

body station. A general sketch of this scheme is shown in Figure 8. The body-fixed coordinate system shown in Figure 8 was chosen because it is independent of the angle of attack.

A second flow visualization technique, using neutrally buoyant helium-filled soap bubbles, was employed for its excellent flow tracing qualities. Each bubble leaves a distinct trace on film of its path past the model. This characteristic is especially valuable in turbulent, separated, or recirculating areas of the flow field, where smaller particles, like those in smoke, typically diffuse into a useless cloud. The bubble technique is used here to aid in qualitative interpretation of the flow field.

3.2 Laboratory Arrangement

A single test section was used for both the laser smoke visualization and the soap bubble experiments. The techniques can be operated simultaneously, but the different lighting requirements preclude any useful enhancement of either technique in combination with the other; consequently, the two visualization techniques were normally used independently. All wind tunnel testing for this investigation was conducted in the Aerospace Laboratory facilities at the University of Notre Dame. The general laboratory arrangement, with the laser equipment in place, is shown in Figure 9.

3.3 Wind Tunnel Models

Three models were selected for the flow visualization experiments and are shown in Figure 10. These models were chosen because they are similar to configurations that have been used in other wind tunnels for static and dynamic experiments at large angles of attack.

3.4 Wind Tunnel

Notre Dame's subsonic wind tunnel is shown in Figure 11. It consists of a set of 12 anti-turbulence screens, a 24:1 contraction inlet, a 2-ft by 2-ft by 6-ft test section, a 14-ft diffuser with an 8.4° expansion angle,

Vortex Mapping Scheme

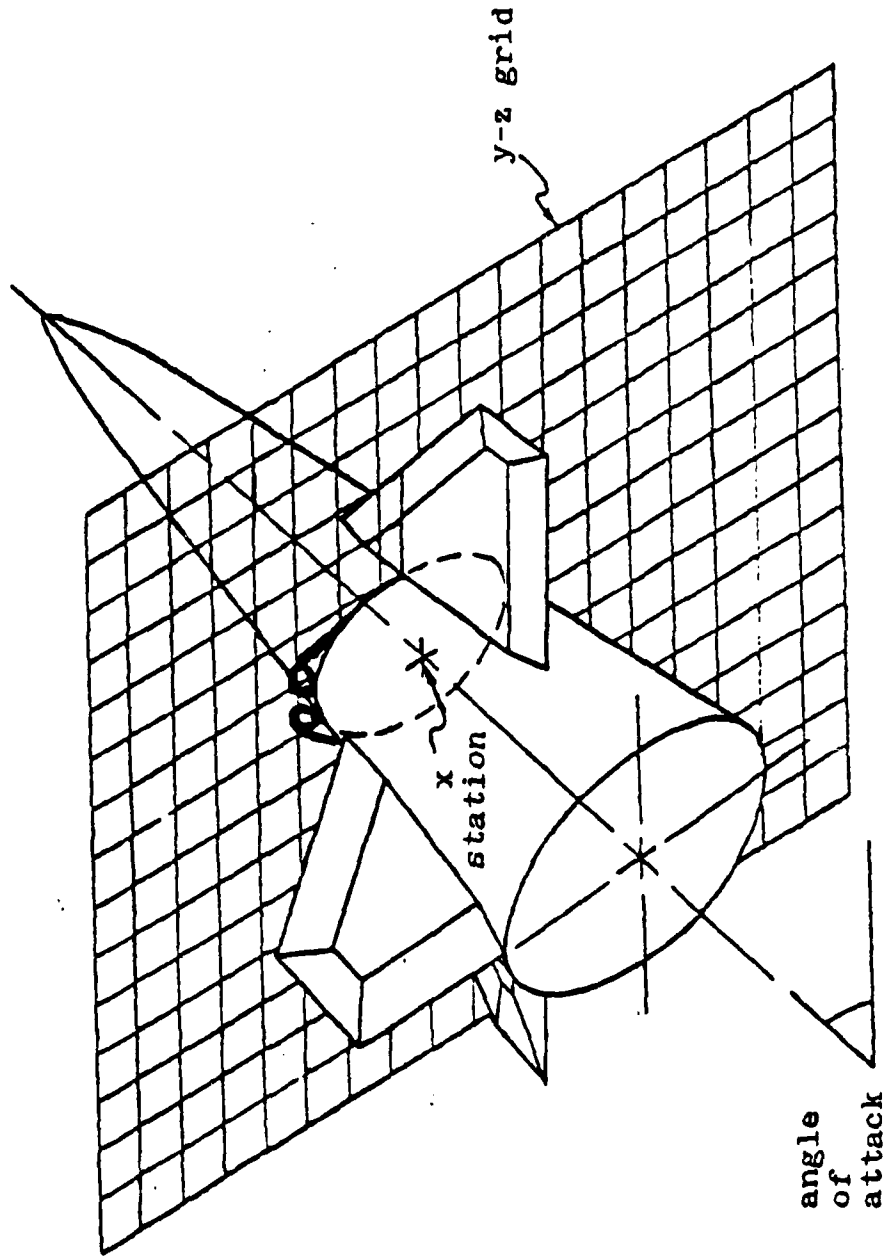


Figure 8. Sketch of Wind Tunnel Model and Grid Scale

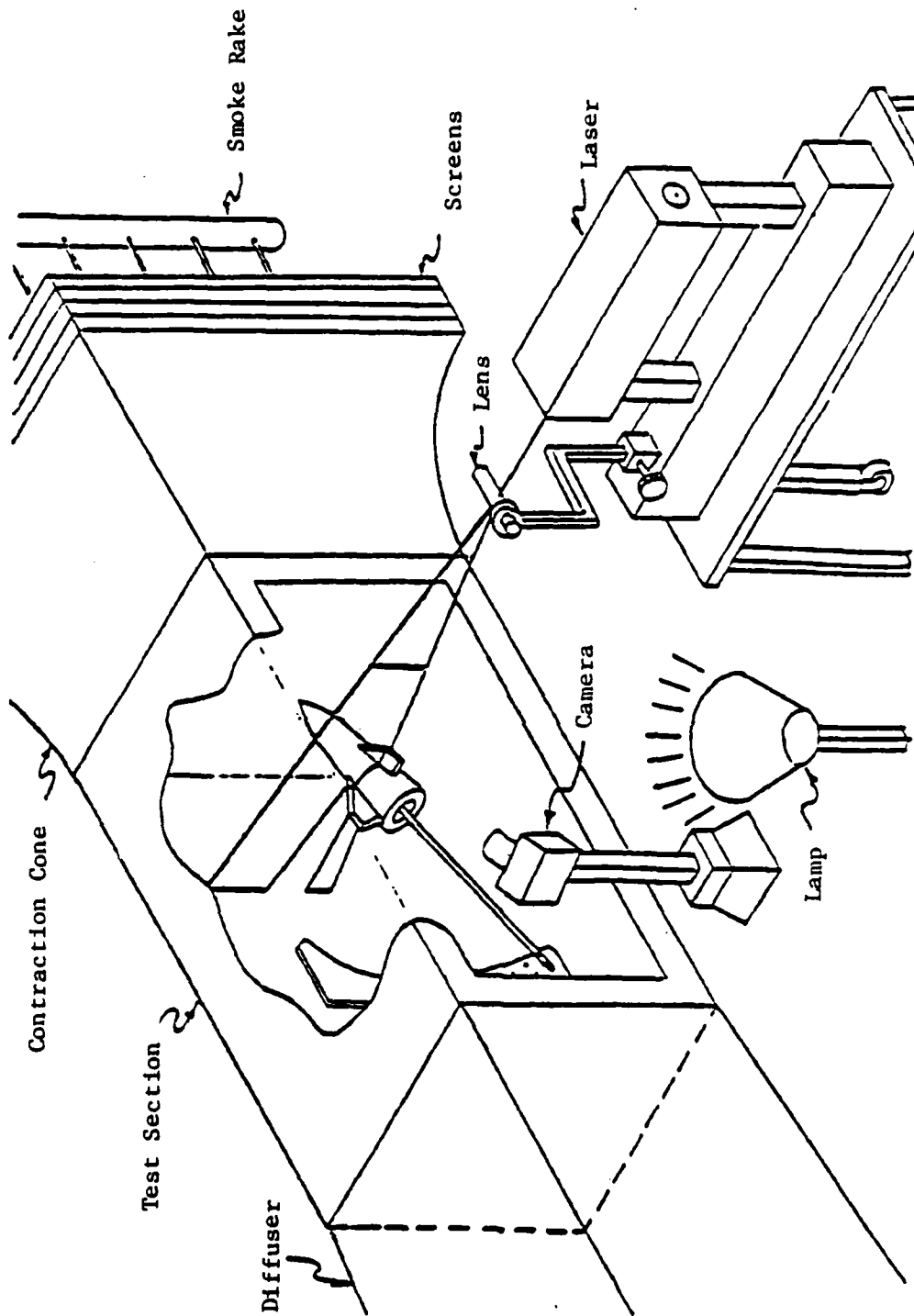
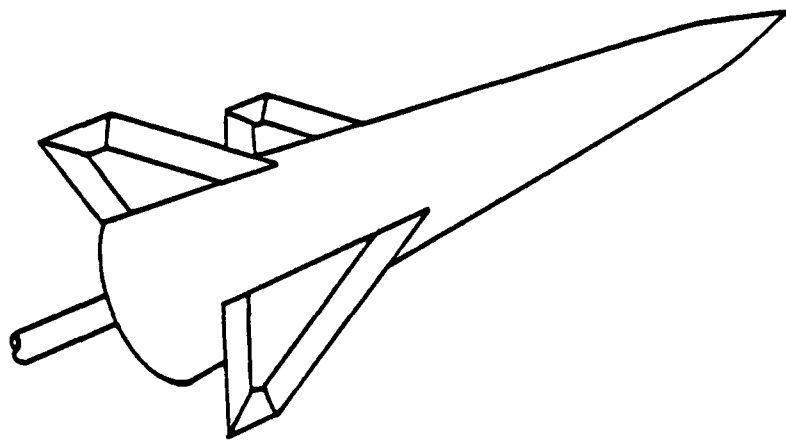
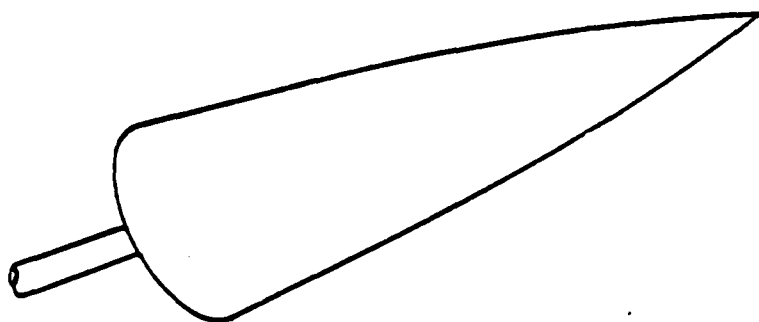


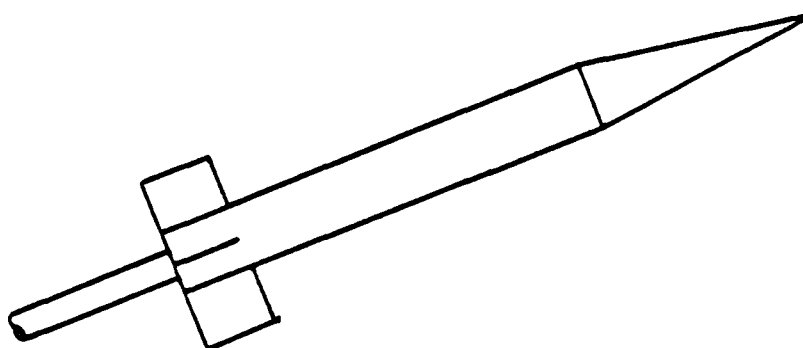
Figure 9. Sketch of Laser and Wind Tunnel Arrangement



NAE Model
 $\lambda = 10.95$ inches
 $d = 3.25$ inches
 $\lambda/d = 3.37$
7° Cone Body - Secant Ogive
Nose
50° Swept Wings and Vertical

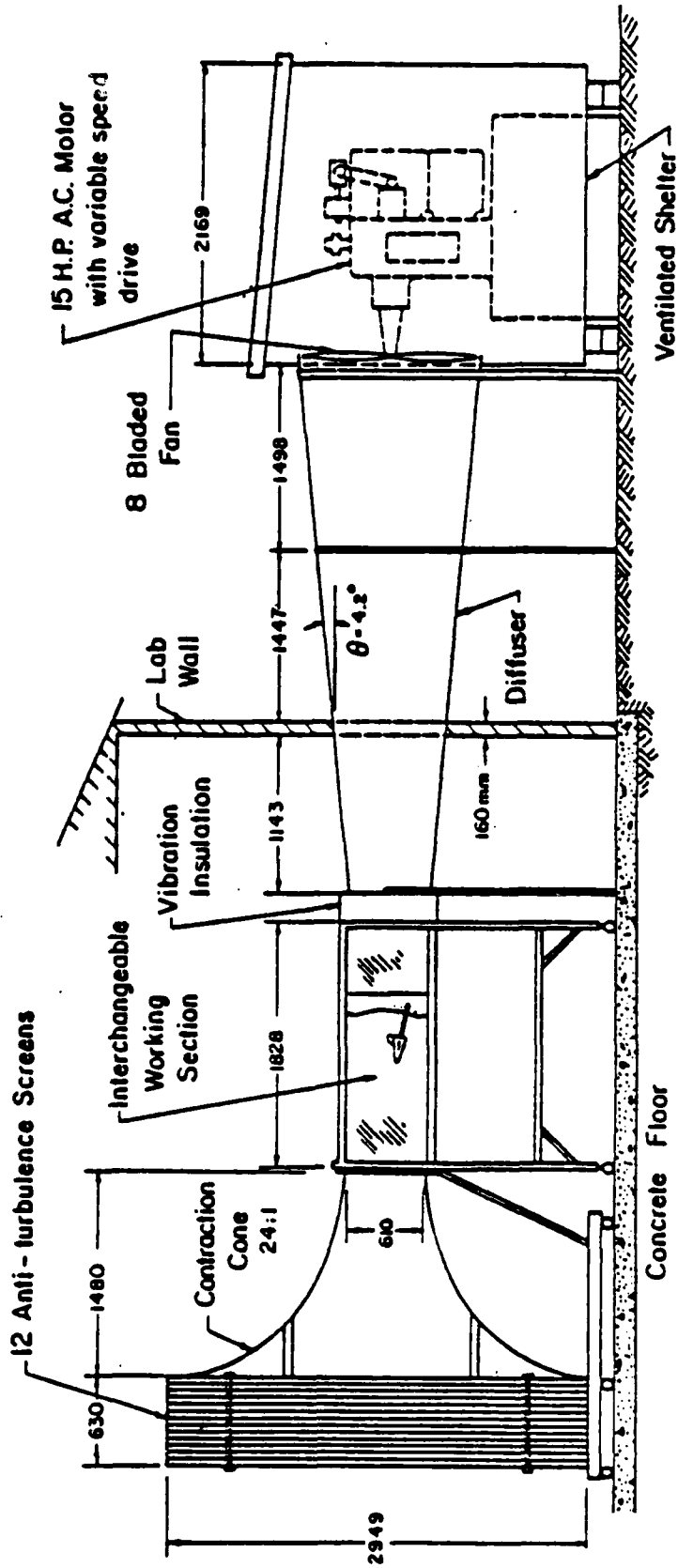


Tangent Ogive Model
 $\lambda = 12$ inches
 $d = 3$ inches
 $\lambda/d = 4$



Basic Finner Model
 $\lambda = 12$ inches
 $d = 1.2$ inches
 $\lambda/d = 10$
3 Caliber Conical Nose
Square Flat Plate Tail
Surfaces $d \times d$

Figure 10. Flow Visualization Models



All dimensions in millimeters.

Figure 11. University of Notre Dame's Subsonic Wind Tunnel

and an eight-bladed fan driven by a 15-hp variable speed AC motor. The maximum operating velocity is 90 ft/s in a 4-ft² test section. Data for this experiment was taken at velocities between 30 and 90 ft/s, although most of the photographs were taken at the lower end of this range.

The test section has glass on one side, a window on the bottom, and the opposite interior walls are flat black. The sting support for the model can be set at angles of attack from 0 to 55 degrees in a movable mount on a vertical plate in the center of the test section. Although the normal turbulence intensity in the test section is about 0.1 percent, various higher turbulence intensities can be induced by placing screens of different mesh sizes at the upstream end of the section, at the joint between the inlet and the test section.

3.5 Smoke Generation

Smoke for this experiment was produced by dripping kerosene onto strip heaters in a four-tube smoke generator, shown in Figure 12. A blower forces the resulting dense white smoke into a smoke rake where it is cooled in a series of heat exchangers and passed through a cloth filter bag. A sketch of the smoke rake is shown in Figure 13. The smoke can then be separated into tubes of equal spacing, or, as was sometimes found to be more practical in this study, the smoke may be formed into a single large tube by being diverted into a set of fine mesh screens and a bell mouth similar to the contraction cone of a wind tunnel. The smoke is introduced in front of the anti-turbulence screens, and its passage through the test section can be adjusted by moving the smoke rake vertically or horizontally. This feature is important in getting the smoke to impinge properly on the model to achieve the best flow visualization. Smoke is used only once, and is then exhausted outside the laboratory.

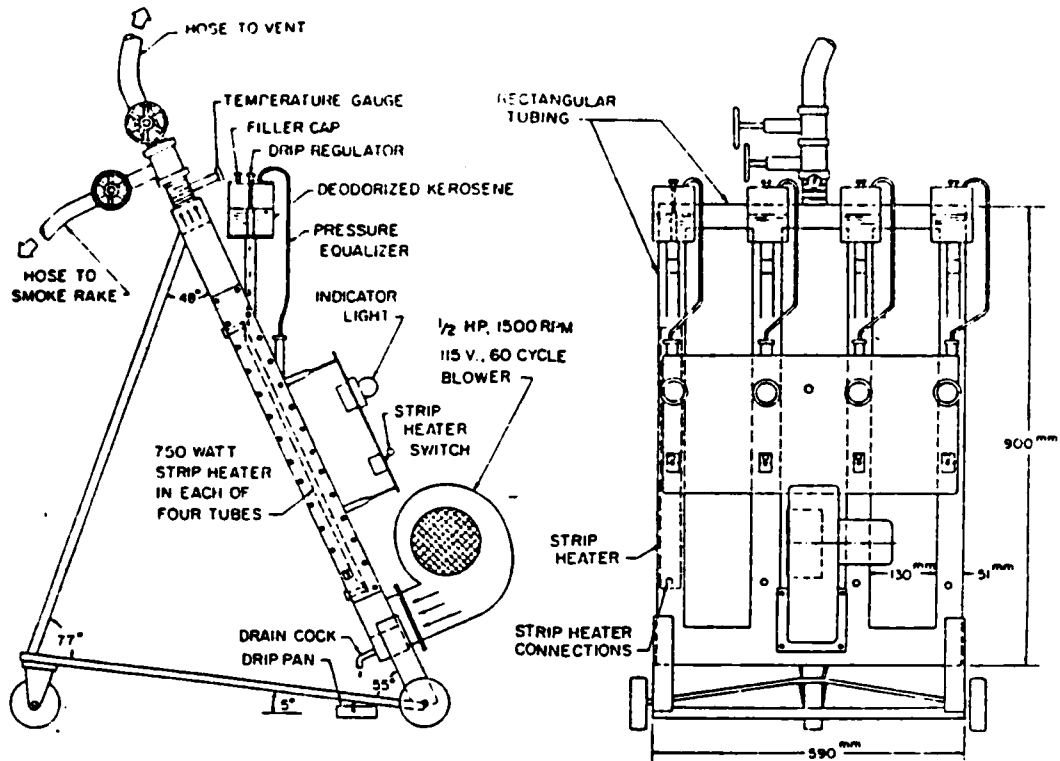


Figure 12. Smoke Generator

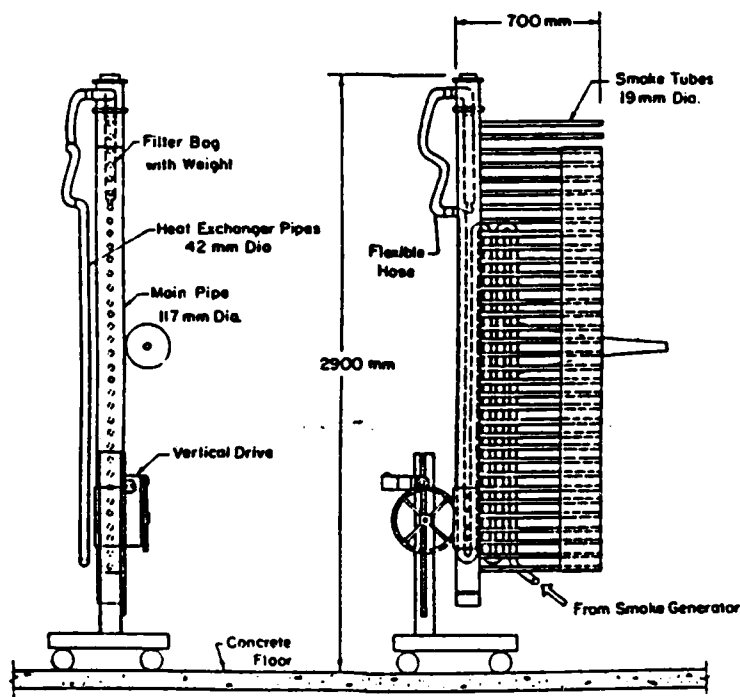


Figure 13. Smoke Rake

3.6 Sheet of Light

The laser method for creating a sheet of light is shown in Figure 14. A bright red laser beam is produced by a Spectra-Physics Model 120 5mW helium-neon laser, powered by a Spectra-Physics exciter. This beam is sent through a cylindrical glass lens. When the incident beam is perpendicular to the cylinder axis and centered on the lens, the beam will be diffused into a plane which is also perpendicular to the cylinder axis. This is especially convenient in that to produce a sheet of light perpendicular to the model axis, one need only make the model and cylinder axes parallel.

Most of the beam's diffused light energy is concentrated within an angle of less than 5° . This relatively narrow strip can be raised or lowered through at least 45° by raising or lowering the lens a very small amount. Because of this sensitive alignment between laser and lens, both are mounted on the same support rail. The entire support table is on wheels, and can be rolled on the floor to position the laser sheet at the proper axial location on the model. The right angle between the sheet and the longitudinal axis of the model can be preserved by ensuring that the portion of the laser sheet reflected by the test section window passes back into the incident sheet.

3.7 Bubble Generation

The neutrally buoyant helium soap bubble generating system, manufactured by Sage Action, Inc., is shown in Figure 15. Its console has external connections for helium and air supplies, a one liter reservoir for bubble film solution, and sets of output connections, quick shutoff toggle valves, and micro-metering valves for each constituent. The console has independent controls for up to three bubble generating heads. Three parallel lengths of plastic tubing carry the air, helium and film solution

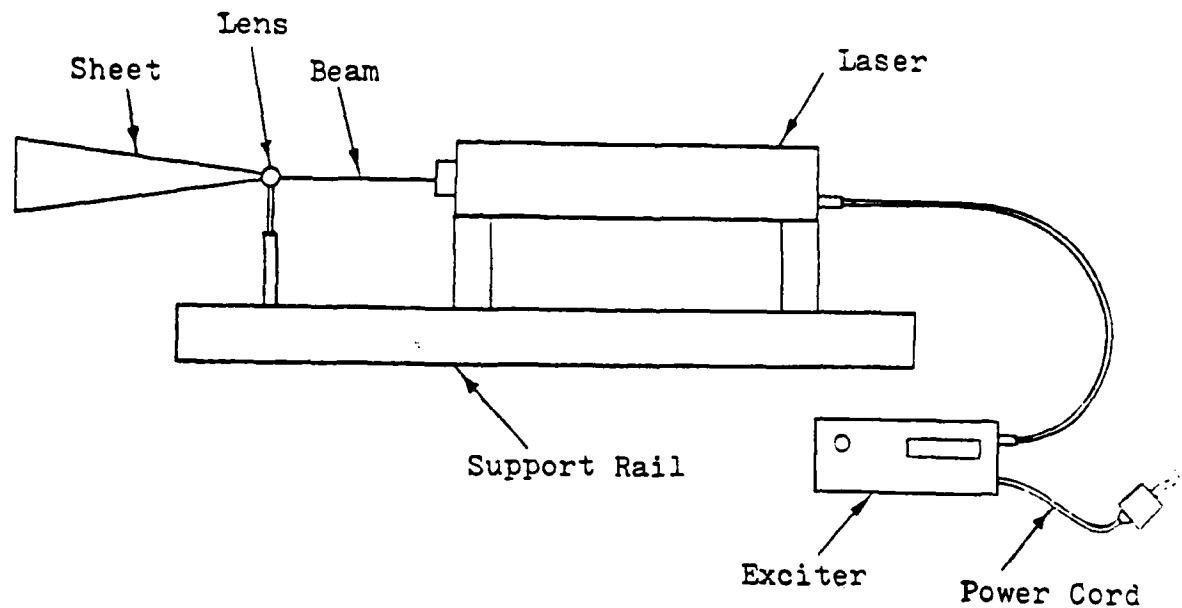


Figure 14. Laser and Lens Set-up

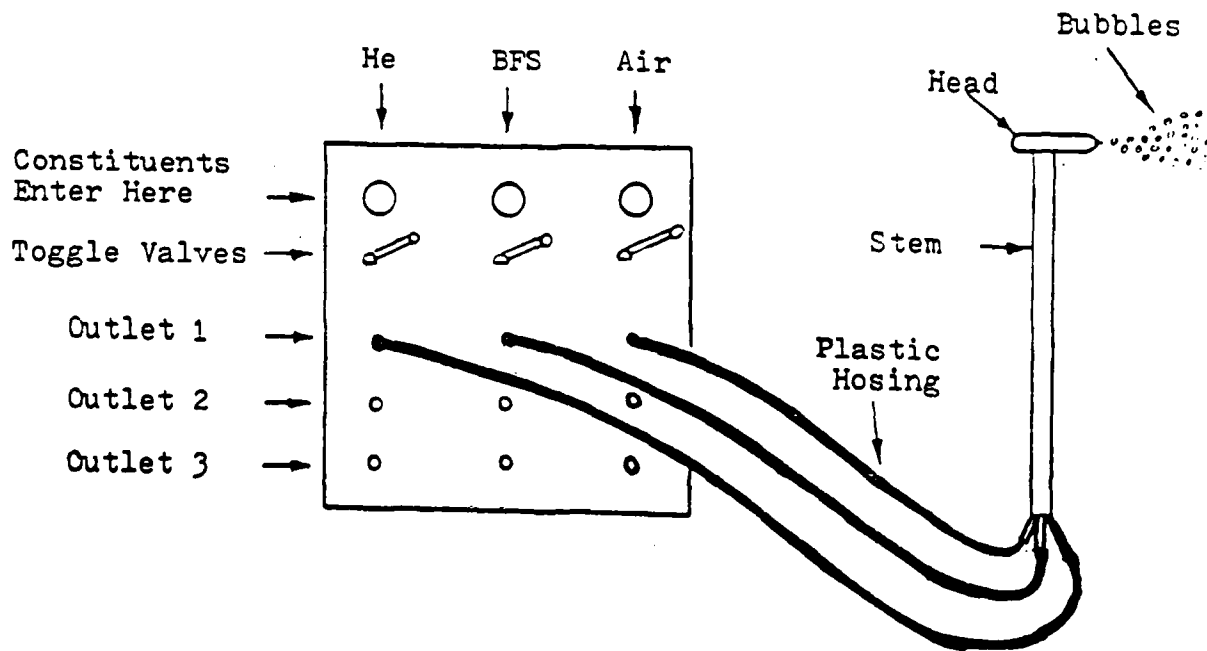


Figure 15. Bubble Generator

to connections at the base of the brass support stem for the head, which then forms and injects bubbles into the airflow upstream of the model.

In operation, pressure from the external supplies forces the constituents through three concentric tubes in the bubble generating head. The innermost tube contains helium, which fills the bubble formed by film solution in the annulus around this tube. Air in the outer shroud blows the bubbles off the tip as they are formed. With the proper external pressure settings and careful manipulation of the micro-metering valves on the console, the buoyancy, size, and generation rate of the bubbles can be controlled. Bubble generation rates of as high as 500 bubbles per second can be achieved, and each bubble has a minimum lifetime of 30 seconds. Bubbles may be implanted into air streams at speeds from 0 to over 200 ft/sec.

3.8 Lighting

Various lighting techniques were used to achieve different visual objectives. With the smoke and laser setup, floodlights or strobe lights are best for viewing the smoke and model alone, but completely drown out the laser sheet. Total darkness, on the other hand, is best for observing the laser pattern, but the model is nearly invisible as a reference. The use of moderate room lighting or wall-reflected floodlighting permits a good view of the model, smoke, and laser pattern simultaneously, at the expense of some quality in both smoke and laser visualization. This compromise is small, and such intermediate lighting is used extensively for the laser experiments.

For the helium bubble technique, strong floodlighting is required to compensate for the low reflectivity of the bubbles. As before, floodlighting from the general direction of the camera location will obliterate all other subjects in a time-exposure photograph, so the lighting in this case is introduced through the bottom window of the test section. Advantage

can be taken of the model geometry by aligning the floodlight with the model axis such that the model's base casts a shadow over the forward part of the model. Bubbles are brightly illuminated, while the model is lit by reflected light of much lower intensity.

3.9 Photography

Three different cameras were used in this investigation, each with its own advantages and disadvantages. To exploit the vivid red-on-black contrast encountered in the laser experiments, Kodak Ektachrome Daylight (ASA 400) color slide film was used in a Canon AE-1 SLR still camera. The resulting slides were of excellent quality and were used with a simultaneous projection system to determine the vortex positions.

A Graflex Graphic View still camera with a 210mm, 6.3 f-stop Ilex Acu-Tessara lens was used to obtain 4- x 5-inch black and white negatives. Kodak Royal X Pan (ASA 3000) film was used. The lens and projection surface are independent; thus, oblique focusing problems can be alleviated. This camera can be adapted to use Polaroid Type 57 High Speed (ASA 3000) black and white film, permitting the experimenter to optimize the lighting and exposure with one or two trial photographs and processed immediately before exposing any negatives. Complete processing to print form is inexpensive and can be quickly performed in a darkroom facility. This allows the use of darkroom 'dodging' techniques to enhance contrast and details in the photograph. The final prints obtained using this method are clear, sharp, and suitable for reproduction. Their shortcoming lies in the fact that the red laser sheet and white smoke appear to be the same color, and are not always readily distinguishable from one another. This is not a problem with the helium bubble experiment, in which the white bubbles and the black model are the only two colors present.

In an attempt to aid in the overall qualitative analysis, motion pictures were also taken, of both the laser and bubble experiments. The camera used was a Bolex H16 Rex 16mm movie camera, with Kodak B and W 4-X (ASA 500) negative movie film. These movies can yield important sequential information, but are limited in exposure times and required lighting levels.

For any of the three photographic setups, a sturdy tripod mount is used, having three-axis rotation, with locks to preserve settings. These features are essential in being able to produce identical camera views for several series of photographs. In general, the camera placement depends on the visualization technique.

For the laser technique, since the laser light scattered by smoke particles is mostly returned toward the incident sheet, a camera position close to the sheet would seem desirable; however, positions too close to the sheet cause distortion of the laser pattern in the final pictures. Positions that are nearly facing the sheet do not receive enough scattered laser light to be usable. Thus, oblique camera angles (30 to 60 degrees from the incident sheet) yield the best photographs for the laser experiment.

For the bubble technique, the bubbles must remain in the camera's field of focus as they pass the model to produce fine streaks on the photograph. Therefore, camera positions facing the flow from the side are necessary, and the higher the f-stop, the better the quality of three-dimensional flow pattern photographs.

3.10 General Procedure

A typical experiment involved a "dry" run during which the visualization system in use was fine tuned to best highlight the area of the flow under scrutiny. During this checkout, different lighting arrangements were tried, reflections in the test section window that might enter the camera's field

of view were eliminated, and the procedure for taking one photographic sequence was timed, to help estimate how long the actual experiment would take. For the genuine photographic run, the camera settings, model position, freestream flow conditions, lighting arrangement, and any special remarks about the objective of the photograph were recorded in a log immediately after the photograph was snapped.

The laser sheet of light position is more readily changed than the model's angle of attack, so the normal procedure was to photograph the laser pattern at several body stations for one angle of attack at a time. For convenience, these body stations were the same as for the vortex mapping described below, although some photographs were taken at intermediate positions when something unusual was visible. For the models used here, experience shows that the vortex pattern becomes asymmetric at above 40° angle of attack. It was considered satisfactory, then, to photograph two angles of attack with definitely symmetric patterns (25° and 35°) to show trends before the onset of asymmetry, and three angles of attack (45° , 50° , and 55°) to show successive stages in the development of the asymmetric arrangement. The patterns were photographed both in color and in black and white.

3.11 Vortex Mapping

The vortex mapping procedure was performed only for the NAE model. Since the experimental results must provide a comparison of vortex positions for various angles of attack, it was decided to make the photographs for this portion of the experiment independent of the angle of attack. In other words, the camera orientation was changed for each angle of attack such that the model maintained the same position in every photograph. In effect, the camera was always in the x-y plane of the model and positioned to its rear quarter.

From experience, it was considered sufficient to record the laser patterns at three x stations for each angle of attack. Tiny reference dots were made on the model at points 3, 5 and 7 inches from the nose. A fourth station located 9 inches from the nose was unusable due to the diffusion of the smoke in the vicinity of the horizontal wings. Photographs were taken at angles of attack of 25°, 35°, 45°, 50° and 55°. A total of 15 photographs was therefore necessary.

For each pattern, the laser sheet was first aligned at the x station reference dot, and then the smoke was adjusted for the best definition of both vortex cores. The location of the smoke rake upstream of the contraction cone made this adjustment easier, since a relatively large movement of the rake corresponds to a small change in the position of the smoke in the test section. The camera lens aperture was kept at the fully open position to allow the shortest exposure times, thus minimizing any blurring effects due to turbulence in the flow. Even so, repetitive photographs were possible of most patterns, since the flow field remained steady at all but the highest angles of attack possible on the sting support.

A set of y-z grid photographs was made, with the smoke, laser and wind tunnel all turned off. Since the laser photographs were independent of the angle of attack, only three grid photographs were necessary, one for each x station. A stiff cardboard grid of squares 0.1 inch on a side had a hole cut in it to fit the model at the first x station, and it was secured on the model in the test section. It was photographed under medium floodlight conditions from the same camera position as when the laser pattern was photographed. The hole was then enlarged to fit the next x station, and the photography was repeated. The third station was photographed in the same manner, except that an extra slot had to be cut to accommodate the beginning of the wing fins. Table 4 lists the appropriate

geometric information for each x station.

Two methods were used for the actual determination of the y and z coordinates of each vortex core. For the symmetric angles of attack, a laser pattern slide and the corresponding scaling grid slide were simultaneously projected using independent slide projectors. The alignment was made by exactly overlapping the images of the model from each slide. The y and z coordinates could then be read directly from the projection screen.

For the asymmetric angles of attack, the scaling grid negative was projected onto a photographic print of the laser pattern. The model images were aligned in a similar manner as above, and the y and z coordinates were again directly determined.

TABLE 4. GEOMETRIC DATA FOR SELECTED BODY STATIONS

Station	x (inches)	$\left(\frac{x}{L}\right)$	Radius (inches)
1	3.0	0.27	0.64
2	5.0	0.46	0.89
3	7.0	0.64	1.12

3-12 Bubble Visualization

It was necessary to adjust the helium bubble generating system in still air before performing experiments with it. The generating head was aimed horizontally, and the bubbles being blown off the tip were adjusted for the desired size. The helium and film solution content of the bubbles were then balanced to produce a cloud of bubbles whose greatest percentage remained neutrally suspended in air. There were always some bubbles that were too heavy or too light, and bubbles occasionally broke during formation at the tip of the generating head. A vortex separating filter is avail-

able for eliminating non-neutrally buoyant bubbles, but was not used in these experiments.

Once adjusted, the bubble head was positioned in the test section, and the tunnel was turned on before the bubble generator to avoid having any bubbles drift onto the side window and burst. As bubbles began forming, the head was moved around until the bubbles were being entrained into the flow region of interest.

Two problems were encountered in using the helium bubble technique that required special procedures to minimize. The first was the accumulation of film solution on the model due to breakage, especially at higher angles of attack. The flow patterns were affected by this accumulation, and thus only one photograph at a time could be taken, and this in a matter of seconds after turning on the bubbles. The model was wiped off after each photograph to try to produce consistent flow fields. The second problem was the danger of overheating the test section glass with the 1000W floodlight. To preclude this hazard, the floodlight was turned on just before a photograph was snapped and then turned off immediately afterward. Also, a cooling fan was directed at the glass in an effort to convect the heat away while the light was on.

Photographs were taken of the primary vortices and of the airflow passing over and around the wing fins. Attempts were also made to photograph the vortices from behind and below the model, and to record the effects of breakage mentioned above.

SECTION IV

DISCUSSION OF EXPERIMENTAL RESULTS

4.1 Vortex Mapping

Several trends in the vortex behavior on the NAE model may be inferred from the vortex mapping data included in Figures 16 and 17. The data was collected by comparing the laser vortex patterns to a set of scaling grids to determine the vortex position relative to the body cross section.

For the symmetric cases, 25° and 35° , the vortex cores rise upward and outward very smoothly along the model. This is due to the strong stability of these configurations, which are virtually unaffected by changes in turbulence or Reynolds number in the ranges tested here. At an angle of attack of 45° , the upper vortex still rises upward and outward, continuing the tendencies of the lower angle cases. The lower vortex, however, begins to move outward and then turns back toward the centerline farther back on the model. This is attributed to the lower vortex filling in the space left by the upper vortex as the latter moves away from the model surface. At 55° , this behavior is much more pronounced. The upper vortex very quickly separates and trails into the freestream, and the lower vortex turns immediately to fill the gap. Then the upper vortex itself starts to return to the centerline, suggesting a tendency toward a tandem arrangement downstream.

These observations are contingent on the premise that the data in Figures 16 and 17 represent the actual trends in the flow field. The possibilities for error are much greater at 45° and 55° , due to: less clearly defined vortex cores, particularly the lower one; dispersion of the smoke into a larger pattern, causing the laser photograph to be dim; probable interference from the tail and wing fins; typically unsteady flow at 55° ; errors in alignment of the scaling grids on the model; and difficulties

in using oblique photography to record planar data. Still, evidence from the flow visualization supports the description of the flow field as given above. The trend of the data is similar to other investigations.

4.2 Laser Smoke Flow Visualization

The flow field for each model was photographed at from three to four body stations at five different angles of attack. In an effort to both consolidate this data and increase the opportunity for qualitative interpretation of the photographs, the results for the various body stations are included in a single figure for each angle of attack. This permits the reader to visualize the development of the vortex patterns along the model. The resulting vortex wake photographs are shown in Figures 18 - 32. The symmetric and asymmetric character of the vortex patterns on all three models at the various angles of attack is depicted in the collection of layer smoke photographs. The patterns on the tangent ogive model are sharper, perhaps due to the slenderness of the model ($l/d = 4.0$) and the absence of fins.

The vortex wake pattern for the NAE model was found to be steady and symmetric at angles of attack below 45° . At 45° , the steady pattern is virtually symmetric on the secant ogive nose portion of the model and then develops into a slightly asymmetrical pattern along the after body. The arrangement at 50° is steady and asymmetric for the whole body, and at 55° , the vortices are unsteady and asymmetric.

The vortices on the tangent ogive nose model behave in a manner similar to the NAE wake structure at all angles except 55° , for which the pattern on the tangent ogive is asymmetric and steady.

For the Basic Finner model the vortex pattern appears to become asymmetric at 35° midway back along the model. At 45° the nose vortices are highly asymmetric with one of the vortices breaking away from the model

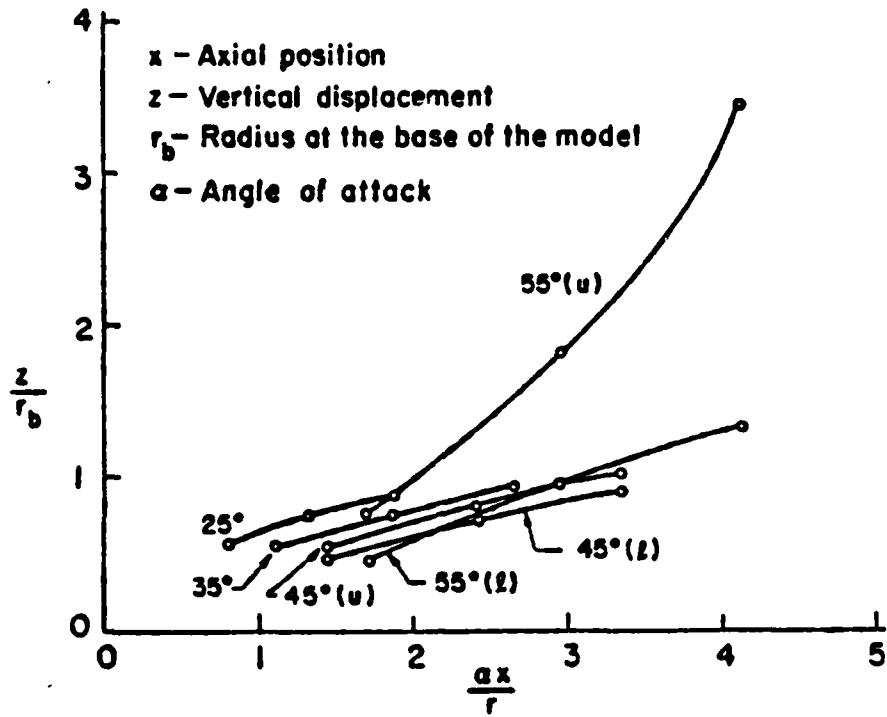


Figure 16. Non-Dimensional Vortex Trajectory Data z/r_b vs. $\alpha x/r$

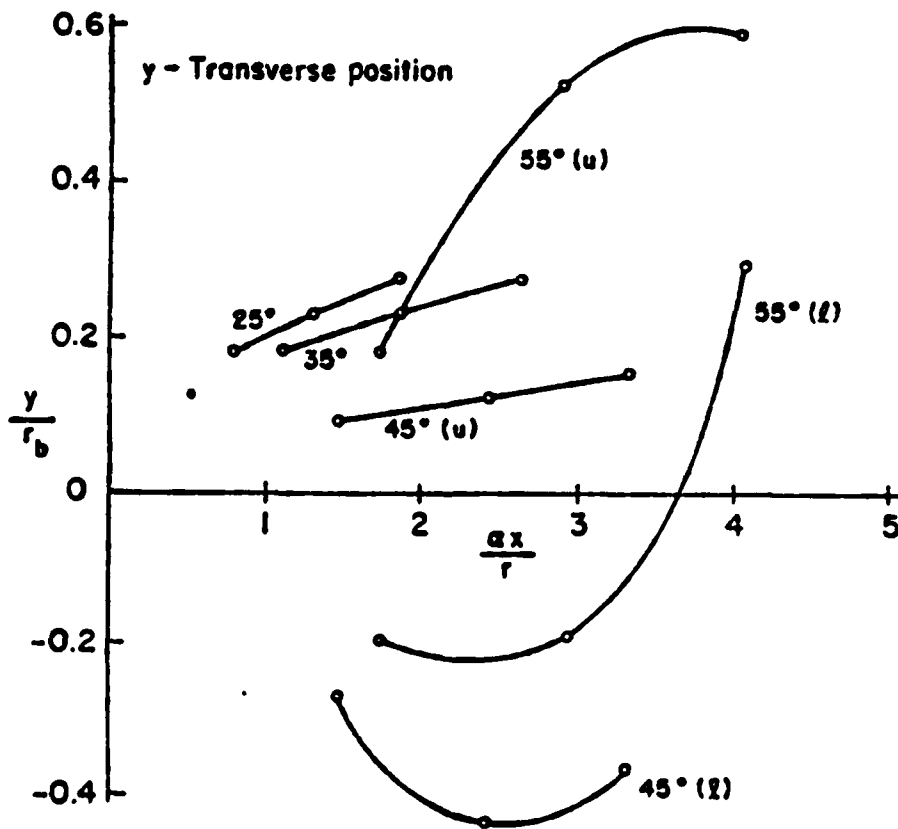
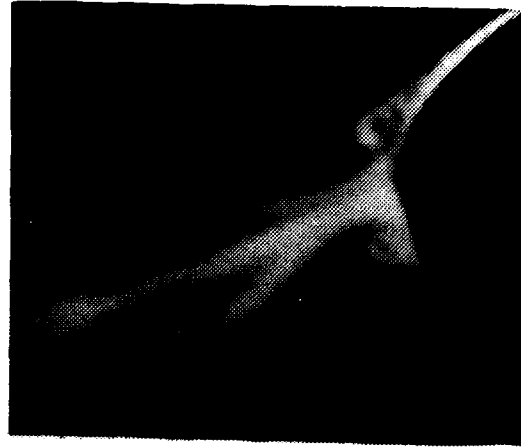
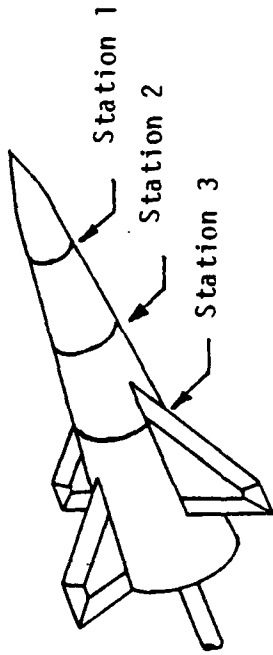


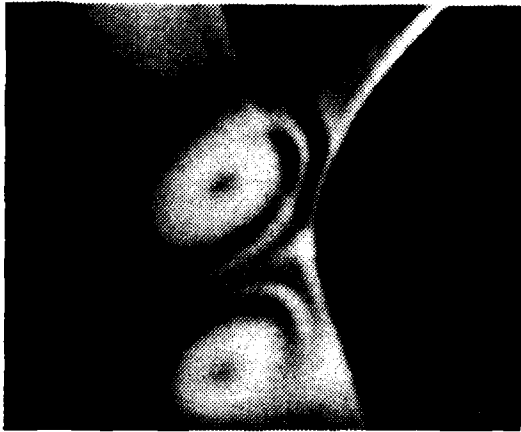
Figure 17. Non-Dimensional Vortex Trajectory Data y/r_b vs. $\alpha x/r$



Station 1

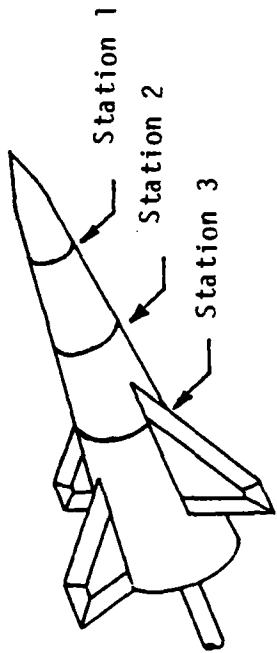


Station 2



Station 3

Figure 18. Vortex Pattern on the NAE Model at $\alpha = 25^\circ$



Station 3

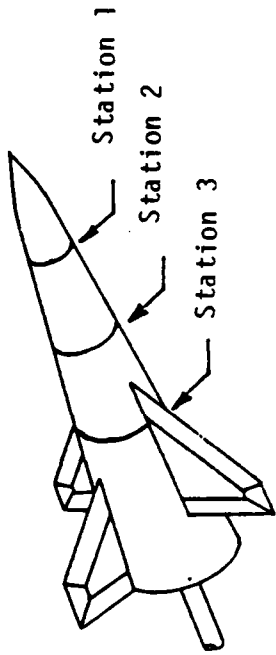


Station 2

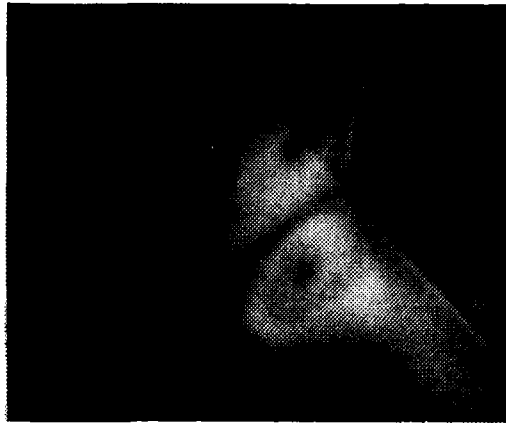


Station 1

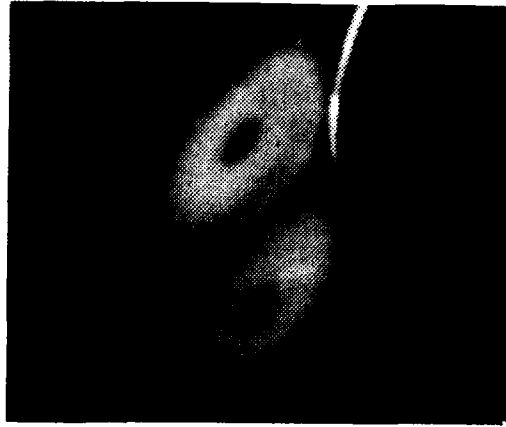
Figure 19. Vortex Pattern on the NAE Model at $\alpha = 35^\circ$



Station 3

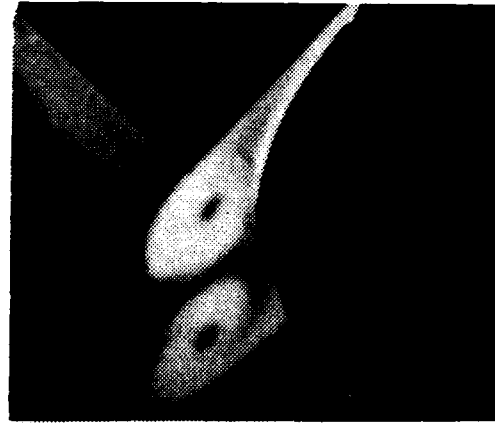
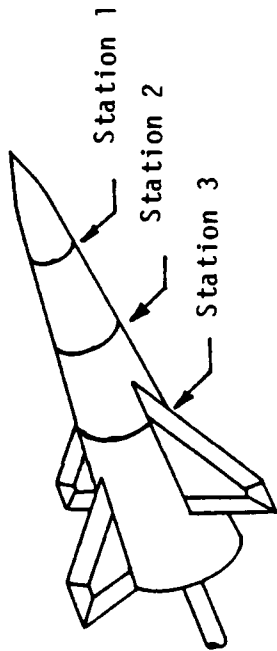


Station 2

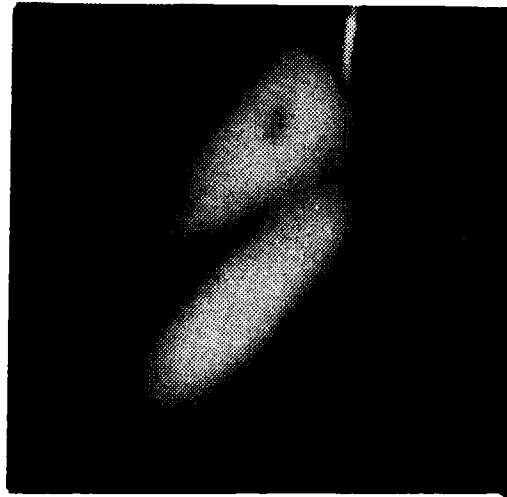


Station 1

Figure 20. Vortex Pattern on the NAE Model at $\alpha = 45^\circ$

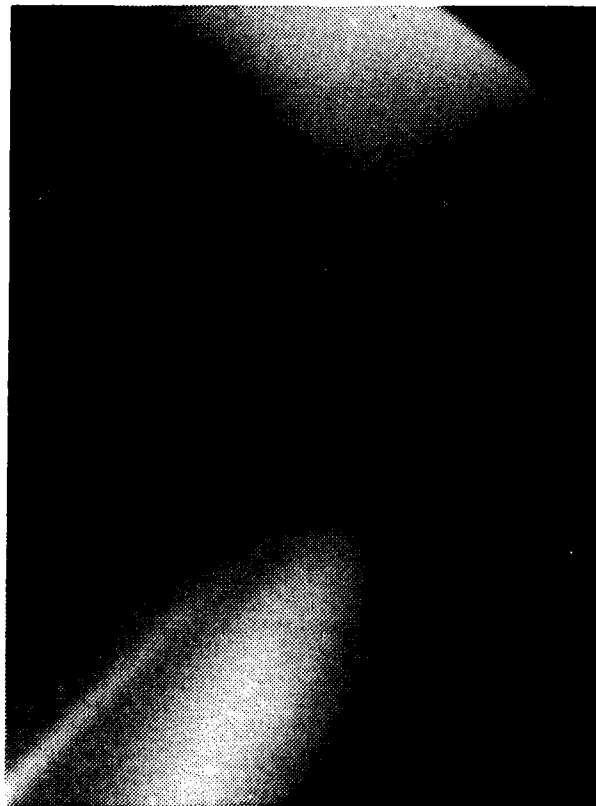
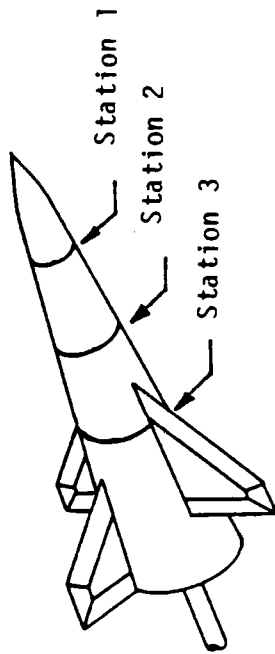


Station 1

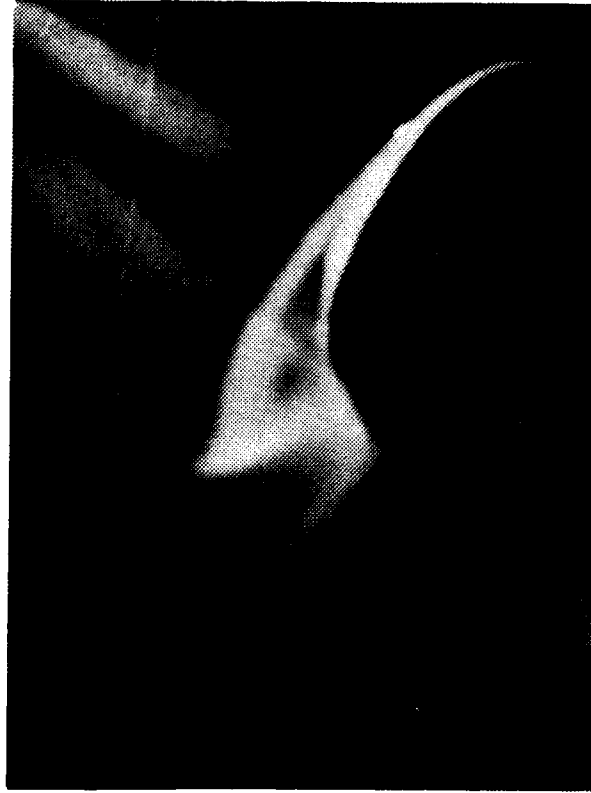


Station 2

Figure 21. Vortex Pattern on the NAE Model 1 at $\alpha = 50^\circ$

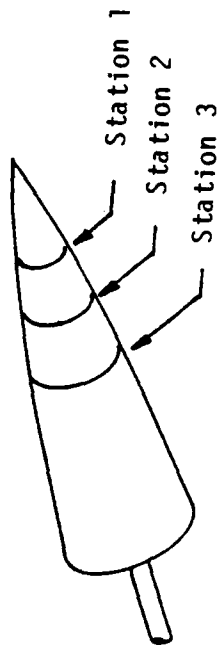


Station 2

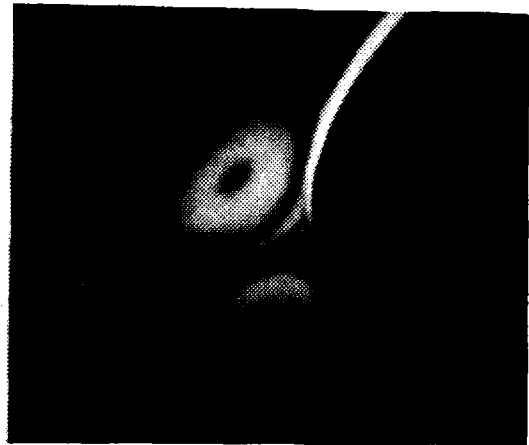


Station 1

Figure 22. Vortex Pattern on NAE Model at $\alpha = 55^\circ$



Station 1

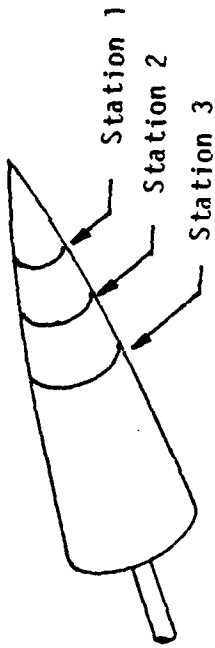


Station 2

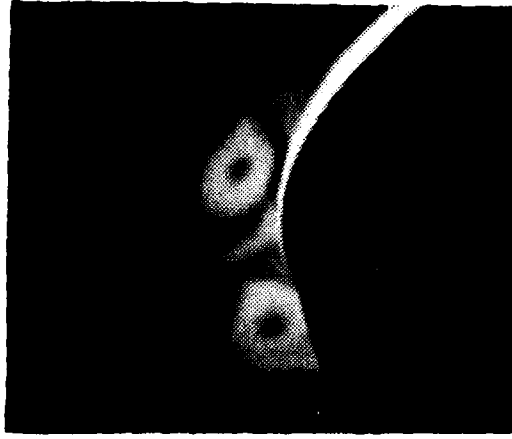


Station 3

Figure 23. Vortex Pattern on a Tangent Ogive Nose Model $\alpha = 25^\circ$



Station 1

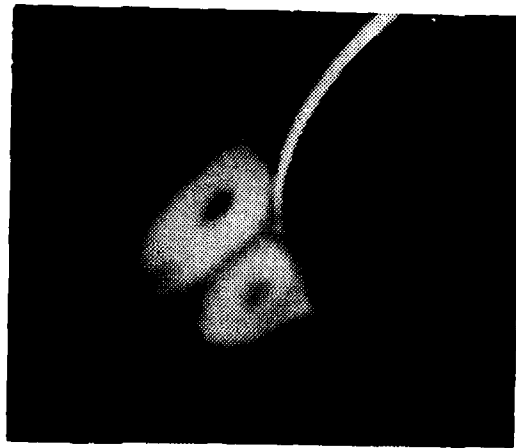
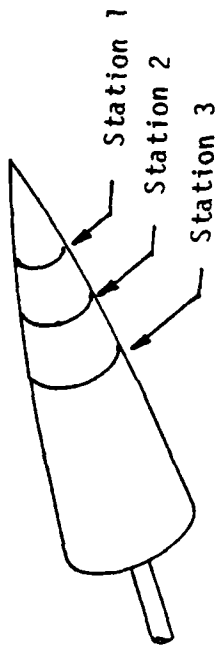


Station 2

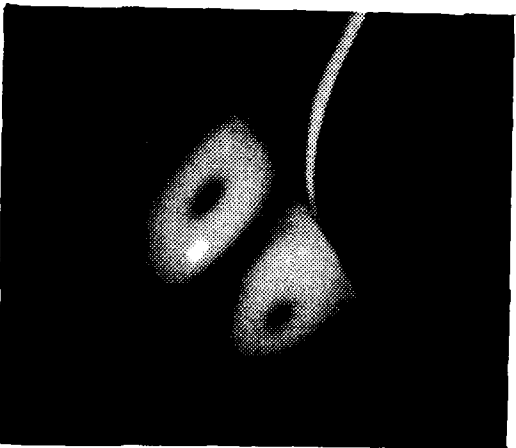


Station 3

Figure 24. Vortex Pattern on a Tangent Ogive Nose Model $\alpha = 35^\circ$



Station 1

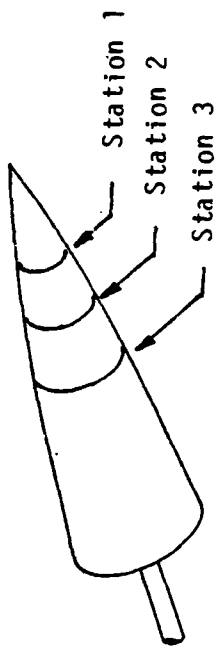


Station 2

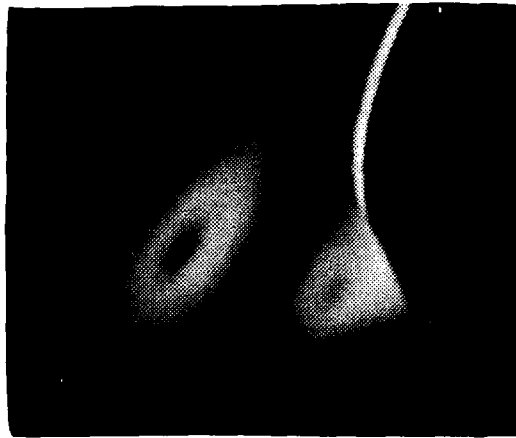


Station 3

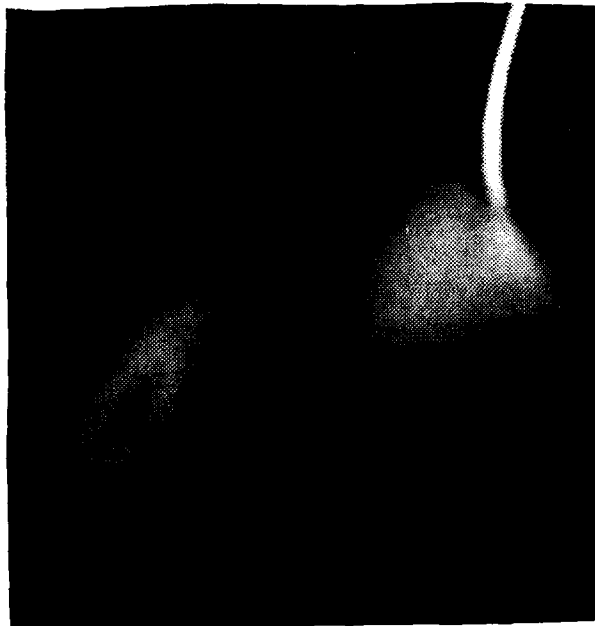
Figure 25. Vortex Pattern on a Tangent Ogive Nose Model $\alpha = 45^\circ$



Station 1

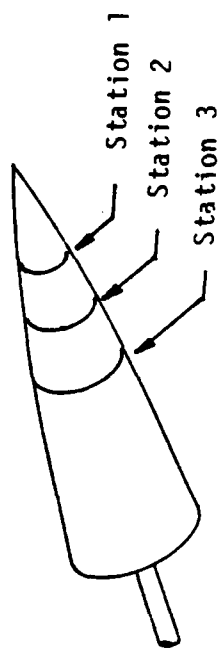


Station 2



Station 3

Figure 26. Vortex Pattern on a Tangent Ogive Nose Model $\alpha = 50^\circ$

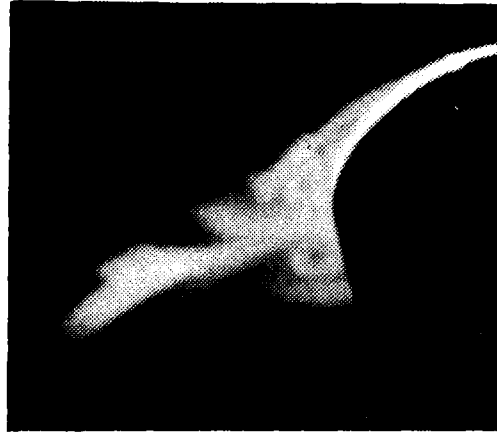
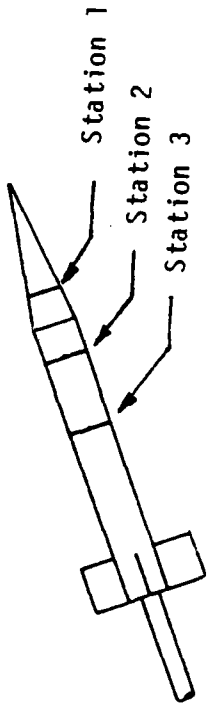


Station 1

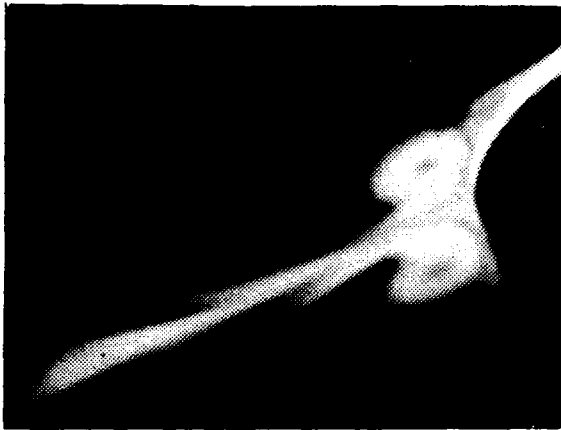


Station 2

Figure 27. Vortex Pattern on a Tangent Ogive Nose Model $\alpha = 55^\circ$



Station 1

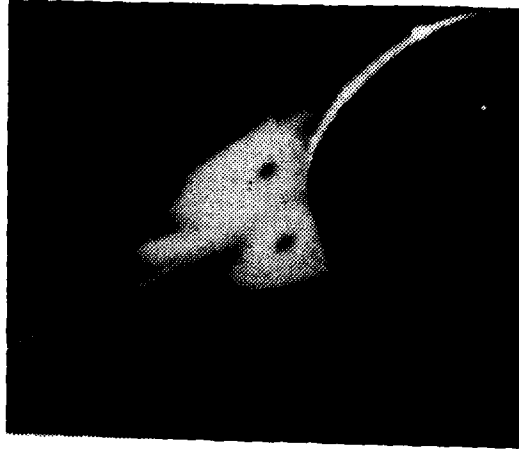
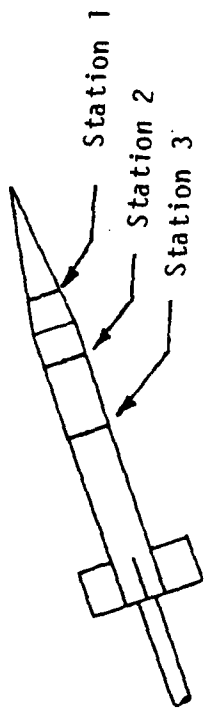


Station 2

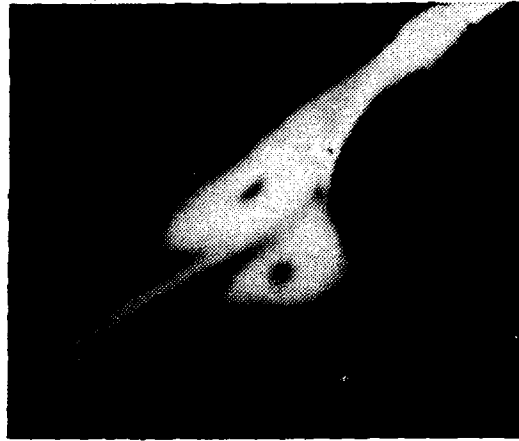


Station 3

Figure 28. Vortex Pattern on the Basic Finned Model $\alpha = 25^\circ$



Station 1

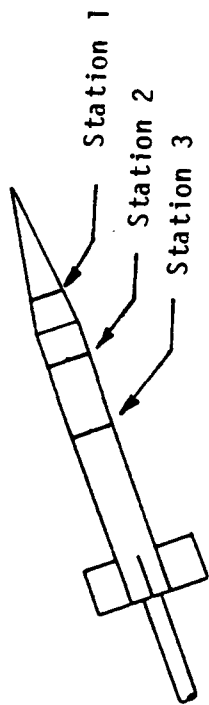


Station 2

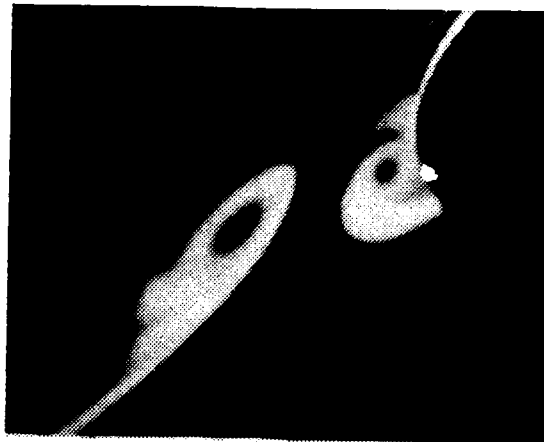


Station 3

Figure 29. Vortex Pattern on the Basic Finner Model $\alpha = 35^\circ$

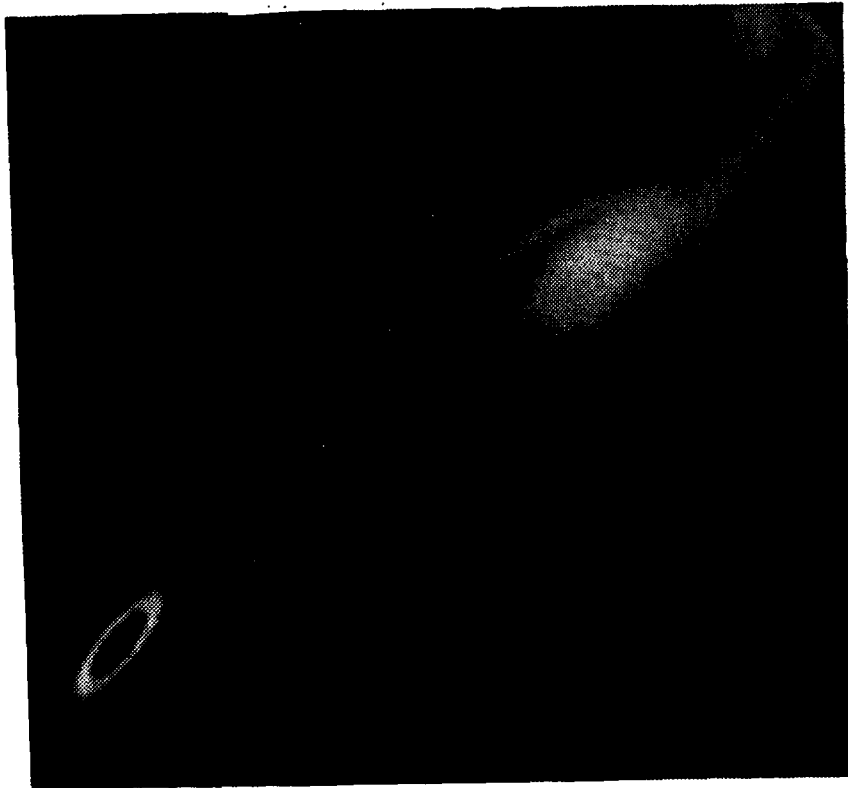
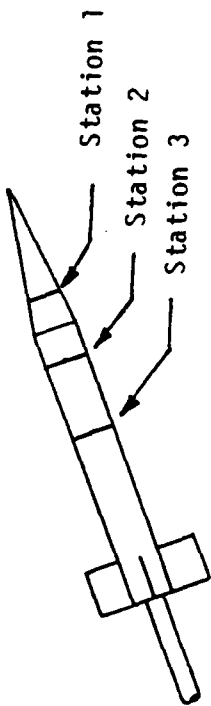


Station 2

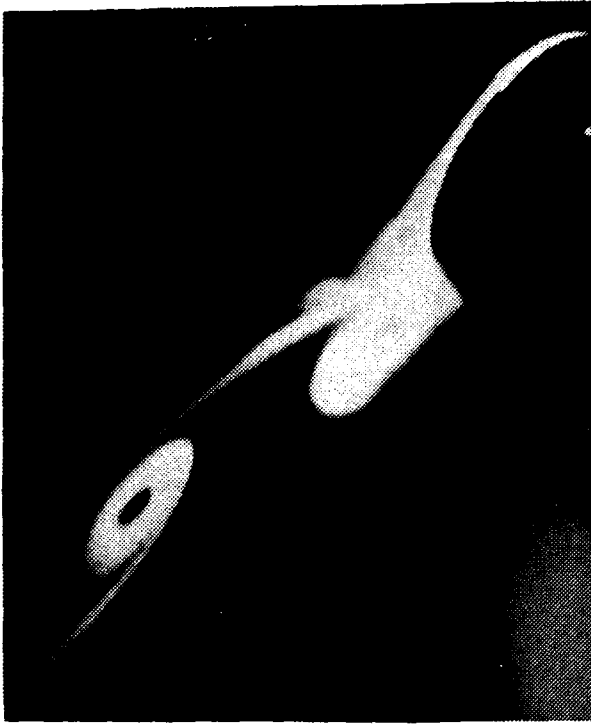


Station 1

Figure 30. Vortex Pattern on the Basic Finner Model $\alpha = 45^\circ$

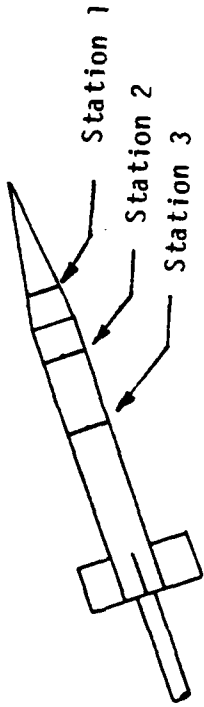


Station 2

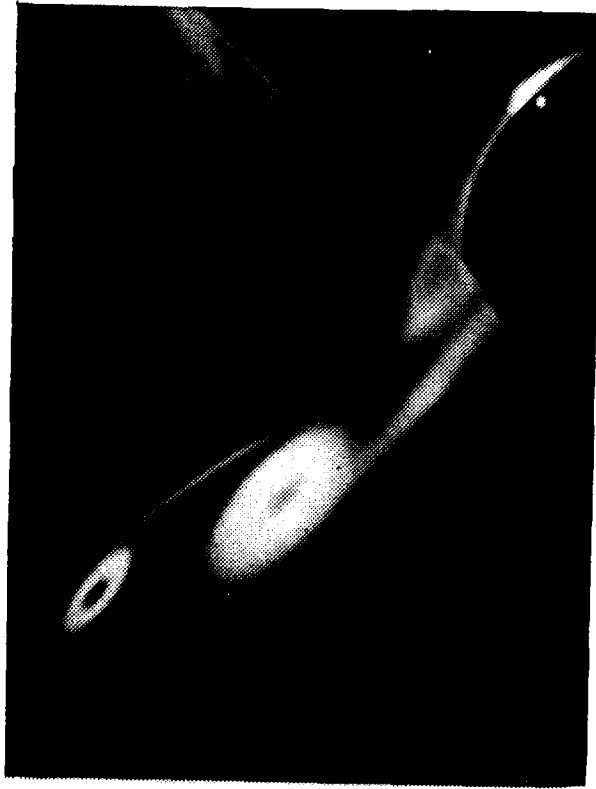


Station 1

Figure 31. Vortex Pattern on the Basic Finned Model $\alpha = 50^\circ$



Station 2



Station 1

Figure 32. Vortex Pattern on the Basic Finner Model $\alpha = 55^\circ$



$\alpha = 50^\circ$

Station #1

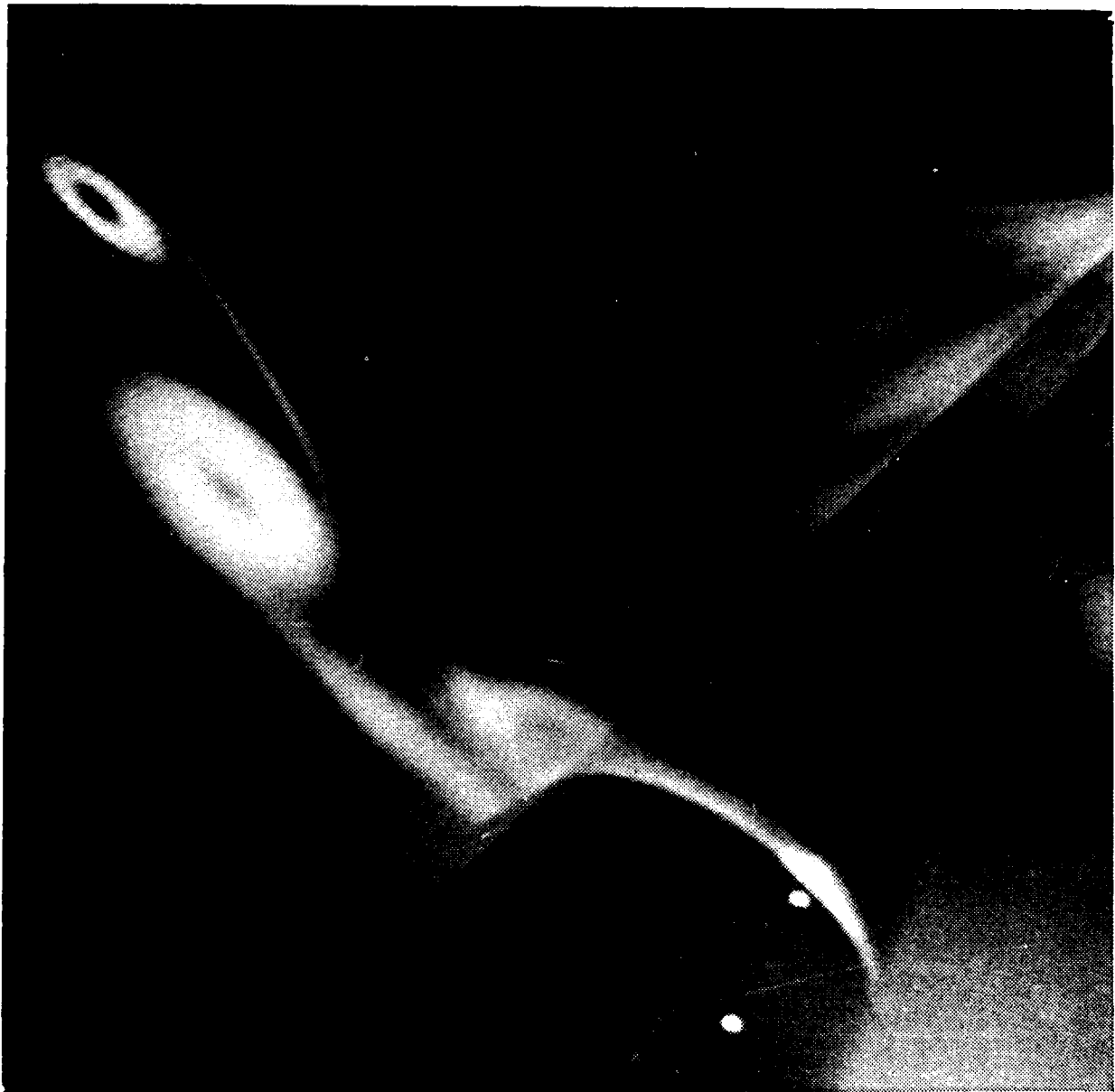
Figure 33. Enlargement of the Vortical Flow Structure on the NAE Model



$\alpha = 55^\circ$

Station #1

Figure 34. Enlargement of Vortical Flow Structure
on the Tangent Ogive Model



$\alpha = 50^\circ$
Station #1

Figure 35. Enlargement of Vortical Flow Structure
on the Basic Finner Model



Figure 36. Helium Bubble Photograph of the Wake
Around the Fins of the NAE Model

before the nose after body juncture. Because the vortices moved away from the body so abruptly, the laser sheet had to be spread through a larger angle which resulted in degradation in photographic quality.

Some of the laser smoke photographs possess exceptional clarity or show evidence of secondary flow characteristics; Figures 33-35 are enlargements of some of the more interesting photographs.

4.3 Helium Bubble Visualization

Photographs were taken of the primary vortices and the airflow passing over and around the wing and vertical fin of the NAE model. Individual flow tracers such as the helium soap bubbles are very useful in some situations. For example, the recirculation region over the wing appears as a cloud of smoke in the laser smoke photographs, yet it is immediately recognizable in the bubble photographs such as Figure 36.

One major difficulty was encountered in using the helium bubble technique. At times the bubbles would break on the windward side of the model, leaving a liquid residue that acted like a flow trip. When the residue became thick enough, the vortex structure was affected significantly.

4.4 Influence of Roughness and Freestream Turbulence

An effort was made to determine qualitatively what effects, if any, might be induced by changes in model surface roughness and freestream turbulence level. At angles of attack for which the vortex arrangement is asymmetric, there is a definite tendency for a particular vortex to be the upper one. The preferred vortex may be the right or the left primary vortex. Whichever configuration developed on the model it could be changed by slight changes in surface roughness near the nose of the model.

Freestream turbulence was changed by adding from one to three turbulence screens upstream of the test section. The magnitude of the turbulence

intensity introduced by each screen is shown in Figure 37.

When the maximum turbulence level was used, the vortex pattern on the NAE model at 55° angle of attack changed from an unsteady to a steady asymmetric pattern.

The tangent ogive nose model was unaffected by the addition of turbulence screens. The patterns at each angle of attack maintain their symmetric or asymmetric character, and the vortex core locations do not change appreciably. The only noticeable difference is an extra fuzziness in the laser patterns when the turbulence screens are in place.

4.5 Assessment of Visualization Techniques

Each of the visualization techniques employed in this investigation is a useful tool, but each also has certain limitations. The laser and smoke system provides an excellent view of the cross-sectional flow pattern, but it requires relatively long exposure times, restricting its use to steady or nearly steady flow fields. To get the best results, expensive color photography must be used.

The helium soap bubble technique produces photographs with good, sharp contrast and detailed information. But unfortunately, the interference problems caused by bubble breakage on the model make it difficult to obtain accurate results. In addition, the macroscopic bubbles may not be following true streamlines. Theoretically, all the bubbles are formed at one point and should therefore describe a single pathline in a steady flow field corresponding to the streamline that passes through the bubble generating head. In practice, however, the bubbles must accelerate from the stationary head to the freestream velocity, and while so doing they have tiny flow fields of their own. The small shedding forces on these bubbles cause them to be sent out from the head in a random, roughly circular array.

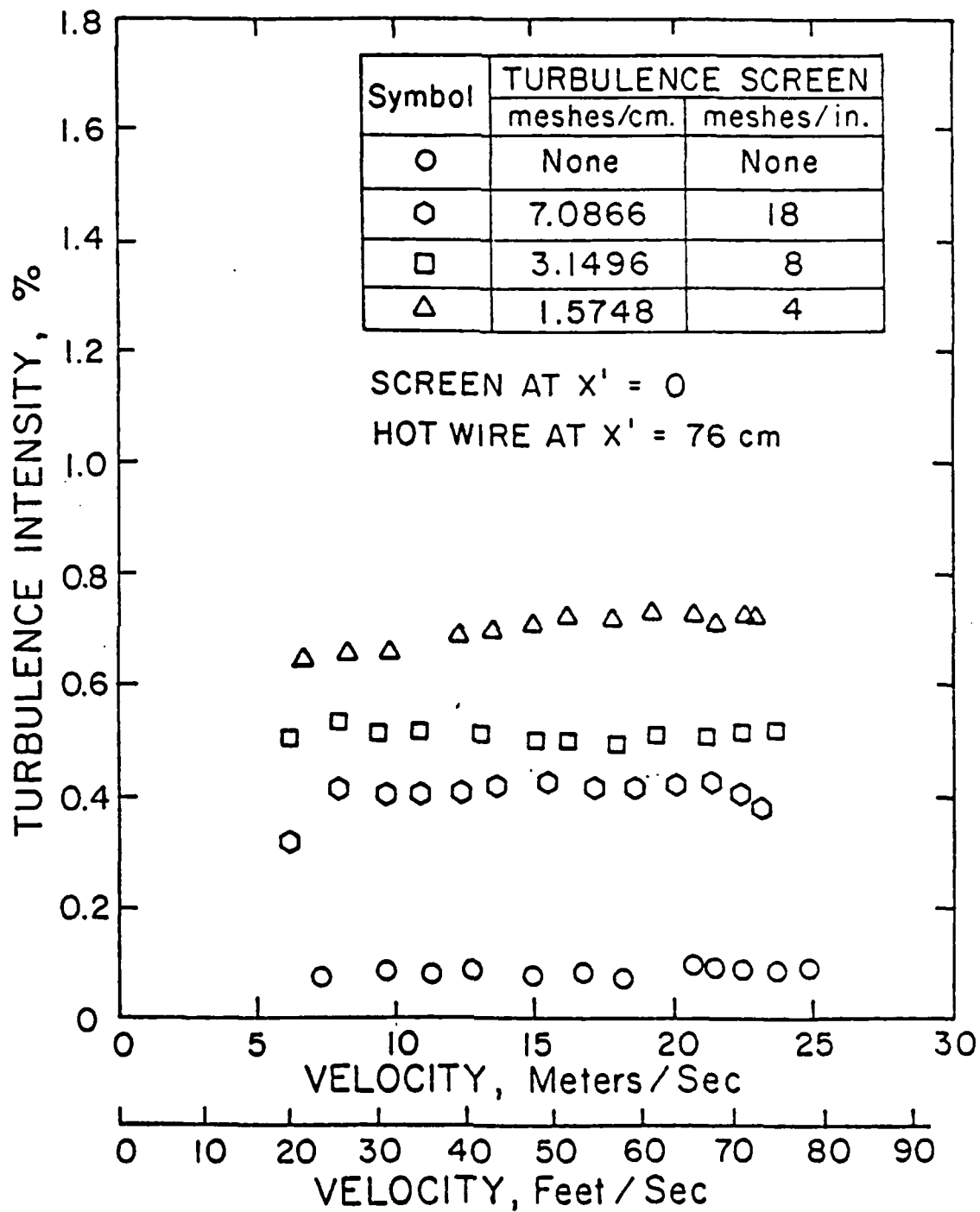


Figure 37. Turbulence Intensity in the Test Due to Wire Screens

Each bubble then has its own pathline, and the image in a photograph is actually a set of pathlines originating from one point, which indicates that the flow field cannot be entirely steady.

The attempts at motion photography are certainly instructive as to the capabilities of such techniques. The movie camera provides a hard copy of sequential information but does not work particularly well in conjunction with the laser smoke visualization technique because of difficulties in lighting requirements. The light around the laser pattern must be dim, while the light entering the camera must be bright.

The vortex mapping scheme is not yet refined enough to produce definitive results. The many possible sources for error cited earlier reduce the reliability of the data significantly. Still, the technique does track the overall behavior of the vortices correctly, and thus it holds some promise for further application.

SECTION V

CONCLUSIONS

Based upon a review of high angle of attack static and dynamic aerodynamic characteristics of slender airplane and missile configurations, as well as the visualization studies documented in this report, the following conclusions were drawn.

When testing for either static or dynamic aerodynamic characteristics, the transitional Reynolds number range (based upon cross flow velocity and body diameter) should be avoided. The flow structure in this range is highly disorganized and has resulted in problems of data repeatability for static tests. Therefore, it only seems reasonable to avoid this range for dynamic testing.

For the visualization experiments carried out as part of this study, the freestream turbulence level was found to affect the leeward wake structure. In the case where the vortex pattern was unsteady, increasing the freestream turbulence level by the addition of turbulence screens caused the pattern to become steady but asymmetric. Therefore, it is concluded that a low turbulence level tunnel is preferable when selecting a tunnel for either static or dynamic aerodynamic experiments at large angles of attack.

The leeward wake structure is very sensitive to support system interference. Therefore, care must be taken to avoid flow distortion due to the sting or support system. In addition, the support system must be as rigid as possible to minimize flow effects due to vibration.

This study, as well as others, has shown how complicated the wake structure on slender models at large angles of attack can be. As indicated in this report, the wake structure and aerodynamic characteristics can be influenced by model fidelity, Reynolds number, and support system

interference. In order to interpret high angle of attack measurements, either static or dynamic, it seems essential that some form of flow visualization be part of the overall research test program. These visualization tests should be carried out on the same model and in the same tunnel for which the static or dynamic aerodynamic tests are conducted.

SECTION VI
RECOMMENDATIONS

The leeward wake structure on slender bodies at high angles of attack is very complex and, therefore, exceptionally hard to model analytically. It consists of a pair of primary leeward vortices generated at the nose and additional body vortices depending on the model configuration and specific body station. Roughness, turbulence, and Reynolds number effects play an important role in determining when and how the primary vortex pattern changes from a steady and symmetric arrangement through a steady and asymmetric pattern to an unsteady and asymmetric case as the angle of attack is increased. The mapping and visualization of these phenomena have been accomplished through the use of several techniques, including laser and smoke cross-sectional visualization and helium bubble flow tracing.

Improvement of Experimental Techniques

There is ample room for improvement in each of the experimental techniques employed in this investigation. The laser-produced sheet of light has good potential for application to unsteady problems if a reasonably instantaneous photograph can be achieved. Possible improvements that may help to reach this goal include the use of a more powerful laser, a lens with a higher transmittance for light than glass, a device for focusing the sheet of light or a rotating prism that sweeps the beam through the plane of interest. Safety considerations should be an important part of any decision to go to a higher-powered laser.

The breakage problem encountered with the helium bubble system can be alleviated by reducing the bubble generation rate and by lowering the air pressure delivered to the bubble head to blow off the bubbles. The latter action, however, may aggravate the bubble scattering problem to the point where too few bubbles are being entrained into the flow region of

interest. A satisfactory compromise between the generation rate and the air pressure can be sought. Alternatively, the use of a vortex separating filter is encouraged for its ability to inject an already moving stream of exactly neutrally buoyant bubbles into the flow.

Extremely high speed movie film is necessary for the successful filming of the laser patterns, particularly if the pattern is unsteady. This requirement may be somewhat relaxed by increasing the effectiveness of the laser system as recommended above. The quality of the laser pattern as reproduced by the video recording equipment is largely dependent on the quality of the hardware itself, which will be proportional to the capital invested in the system. It is advisable to wait for technological improvements in the field of video electronics before committing to this form of motion photography. It is entirely possible that these advances will result in the ability to record laser pattern images that are unsurpassed in the quality of color, detail, and time history when played back on a next-generation video system.

REFERENCES

1. Hunt, B. L., "Asymmetric Vortex Forces and Wakes on Slender Bodies," AIAA Paper 82-1336, August 1982.
2. Chapman, G. T., Keener, E. R., and Malcolm, G., "Asymmetric Aerodynamic Forces on Aircraft Forebodies at High Angles of Attack - Some Design Guides," Paper No. 16, AGARD Meeting on Stall/Spin Problems of Military Aircraft, Ames Research Center, Moffett Field, California, November 18-21, 1976.
3. Lamont, P. J., "Pressure Measurements on an Ogive-Cylinder at High Angles of Attack with Laminar, Transitional or Turbulent Separation," AIAA Paper 80-1556, January 1980 .
4. Lamont, P. J., "The Complex Asymmetric Flow Over a 3.5D Ogive Nose and Cylindrical Afterbody at High Angles of Attack," AIAA paper 82-0053, January 1982.
5. Orlik-Rückemann, K. J., Hanff, E. S., and LaBerge, J. G., "Direct and Cross-Coupling Subsonic Moment Derivatives Due to Oscillatory Pitching and Yawing of the Aircraft-Like Model at Angles of Attack up to 40° in Ames' 6' x 6' Wind Tunnel," National Aeronautical Establishment Technical Report LTR-UA-38, November 1976.
6. Orlik-Rückemann, K. J., "Aerodynamic Aspects of Aircraft Dynamics at High Angle of Attack," AIAA Paper 82-1363, August 1982.
7. Coulter, S. M., and Marquart, E. J., "Cross and Cross-Coupling Derivative Measurements on the Standard Dynamics Model at AEDC." AIAA Paper 81-176, January 1982.
8. "Dynamic Stability Parameters," AGARD FDP Lecture Series, AGARD-LS-114, March 1981.
9. "High Angle of Attack Aerodynamics," AGARD FDP Lecture Series, AGARD-LS-121, March 1982.
10. Ericsson, L. E., and Reding, J. P., "Vortex-Induced Asymmetric Loads on Slender Vehicles," Lockheed Missile and Space Company, Final Report LMSC-D630807, January 1979.
11. Nelson, R. C. and Mouch, T. N., "Cylinder/Splitter-Plate Data Illustrating High α Support Interference," AIAA Journal of Spacecraft and Rockets, Vol. 16, No. 2, pp. 126-128, March-April 1979.
12. Dietz, W. E., Jr. and Altstatt, M. C., "Experimental Investigation of Support Interference on an Ogive Cylinder at High Incidence," AIAA Journal of Spacecraft and Rockets, Vol. 16, No. 2, pp. 67-68, March-April 1979.

13. Uselton, B. L., Haberman, D. R., "Summary of Sting Interference Effects for Cone, Missile and Aircraft Configurations as Determined by Dynamic and Static Measurements," AIAA Paper 82-1366, August 1982.
14. Skow, A. M. and Titiriga, A., Jr., "A Survey of Analytical and Experimental Techniques to Predict Aircraft Dynamic Characteristics at High Angles of Attack." Paper No. 19, AGARD CP 235, Dynamic Stability Parameters, 1978.
15. Erickson, G. E., "Water Tunnel Flow Visualization: Insight Into Complex Three-Dimensional Flow Fields." AIAA Paper 79-1530, 1979.
16. Keener, E. R. and Chapman, G. T., "Similarity in Vortex Asymmetries Over Slender Bodies and Wings." AIAA Journal, Vol. 15, No. 9. 1977.
17. Malcolm, G. N., "The Impact of High-Alpha Aerodynamics on Dynamic Stability Parameters of Aircraft and Missiles," AGARD Lecture Series No. 114 on Dynamic Stability Parameters, Lecture No. 2, March 1981.
18. Schiff, L. B. and Tobak, M., "Some Applications of Aerodynamic Formulations to Problems in Aircraft Dynamics," AGARD Lecture Series No. 16, March 1981.
19. Curry, W. H. and Orlik-Rückemann, K. J., "Sensitivity of Aircraft Motion to Aerodynamic Cross-Coupling at High Angles of Attack," Paper 34, AGARD-DP-235, 1978.
20. Langham, T. F., "Aircraft Motion Sensitivity to Dynamic Stability Derivatives," AEDC-TR-79-11, January 1980.
21. Langham, T. F., "Missile Motion Sensitivity to Dynamic Stability Derivatives," AEDC-TR-80-11, September 1980.

INITIAL DISTRIBUTION

DTIC-DDAC	2
AUL/LSE	1
ASD/ENSZ	1
AFATL/DLODL	2
AFATL/CC	1
HQ USAF/SAMI	1
OO-ALC/MHWRB	1
AFIS/INT	2
HQ TAC/DRA	1
HQ USAFE/DOQ	1
HQ PACAF/DOQQ	2
HQ TAC/INAT	1
ASD/XRX	1
USA TRADOC SYS ANAL ACTY	1
COMIPAC (PT-2)	1
HQ PACAF/OA	1
USA BALLISTIC RESCH LAB	1
AFATL/CCN	1
AFATL/DLODA	1
FTD/SDNF	1
ASD/ENESS	1
HQ USAF/RDQA	1
AFWAL/AADM	1
ASD/XRM	1
NASC (AIR-54113)	1
AD/XRC	1
AFATL/DLMA	10
REDSTONE SCI INFO CENTER	2
AFRPL/MK,MS24	1
AFWAL/FIGX	1
AFWAL/FIMB	1
AFWAL/FIGG	1
ODDR&E/TST&E	1
AEDC LIBRARY	1
NWC (CODE 3905)	1
AFATL/DLMT	1
AFATL/DLJF	1
NWC (CODE 3901)	1
NSWC (CODE K-21)	2
AFATL/DLXP	1
AFWAL/PORA	1
AFRPL/MKAT	1
AFWAL/AART	1
AFWAL/AAWP	1
HQ SAC/XPHA	1

REPROD

FILMED

8

DTIC